AFRL-AFOSR-JP-TR-2019-0011

Novel multi-ferroic nanoparticle-based stretchable composite metamaterials with enhanced magneto dielectric performance

Yuanzhe Piao
SEOUL NATIONAL UNIVERSITY
SNUR&DB FOUNDATION RESEARCH PARK CENTER
SEOUL, 151742
KR

03/14/2019
Final Report

Air Force Research Laboratory
Air Force Office of Scientific Research
Asian Office of Aerospace Research and Development
Unit 45002, APO AP 96338-5002

REPORT DOCUMENTATION PAGE

Form Approved
OMB No. 0704-0188

1. REPORT DATE *(DD-MM-YYYY)*	2. REPORT TYPE	3. DATES COVERED *(From - To)*
14-03-2019	Final	31 Jul 2017 to 30 Jul 2020

4. TITLE AND SUBTITLE
Novel multi-ferroic nanoparticle-based stretchable composite metamaterials with enhanced magneto dielectric performance

5a. CONTRACT NUMBER

5b. GRANT NUMBER
FA2386-17-1-4051

5c. PROGRAM ELEMENT NUMBER
61102F

6. AUTHOR(S)
Yuanzhe Piao

5d. PROJECT NUMBER

5e. TASK NUMBER

5f. WORK UNIT NUMBER

7. PERFORMING ORGANIZATION NAME(S) AND ADDRESS(ES)
SEOUL NATIONAL UNIVERSITY
SNUR&DB FOUNDATION RESEARCH PARK CENTER
SEOUL, 151742 KR

8. PERFORMING ORGANIZATION REPORT NUMBER

9. SPONSORING/MONITORING AGENCY NAME(S) AND ADDRESS(ES)
AOARD
UNIT 45002
APO AP 96338-5002

10. SPONSOR/MONITOR'S ACRONYM(S)
AFRL/AFOSR IOA

11. SPONSOR/MONITOR'S REPORT NUMBER(S)
AFRL-AFOSR-JP-TR-2019-0011

12. DISTRIBUTION/AVAILABILITY STATEMENT
A DISTRIBUTION UNLIMITED: PB Public Release

13. SUPPLEMENTARY NOTES

14. ABSTRACT
Traditional magnetite nanoparticles have a saturation magnetization between 45 emu/g and 55 emu/g due to surface and volume spin canting and defects. However, it has been recently demonstrated that it is possible to improve the saturation magnetization of magnetite nanoparticles by their collective oriented organization in a single nanostructure. The team synthesized corona-shaped magnetite nanostructures that acquire collective assembly during synthesis. Stretchable magneto-dielectric composites were prepared using collectively assembled iron oxide nanostructures as fillers in an elastomer (polydimethylsiloxane) matrix. The resulting composites can be stretched up to 165% strain before failure due to good adhesion between the elastomer and citrate-capped raspberry-shaped nanostructures. A magnetically recoverable photocatalyst was prepared by supporting TiO2 nanoparticles on superparamagnetic raspberry-shaped nanocomposite comprised of a iron oxide nanocluster core@fibrous silica shell. In addition, using raspberry-shaped iron oxides nanoparticles as core material, a carbon nanoshell was further coated by facile methods.
It was demonstrated that raspberry shaped magnetite nanostructures are very interesting and even key elements to fabricate flexible materials with low dielectric loss, high permittivity and permeability values at radio frequencies (1 MHz- 1 GHz). The permeability values achieved by composites made from collectively assembled corona magnetite nanoparticles are significantly higher than the existing magnetite-polymer composites and magnetite-PDMS composites. Additionally, the composites prepared with collectively assembled corona magnetite nanoparticles exhibit an extraordinary magnetic resonance, which changes with the particle size of magnetite nanoparticles. In contrast to these interesting and promising properties of the composites, the composites

15. SUBJECT TERMS
nanocomposite, raspberry shaped particles, magnetic nanomaterials

16. SECURITY CLASSIFICATION OF:			17. LIMITATION OF ABSTRACT	18. NUMBER OF PAGES	19a. NAME OF RESPONSIBLE PERSON
a. REPORT	b. ABSTRACT	c. THIS PAGE			WINDER, SHEENA
Unclassified	Unclassified	Unclassified	SAR		19b. TELEPHONE NUMBER *(Include area code)* +81-42-511-2008

Standard Form 298 (Rev. 8/98)
Prescribed by ANSI Std. Z39.18

Final Report for AOARD Grant FA2386-17-1-4051

Novel multi-ferroic nanoparticle-based stretchable composite metamaterials with enhanced magneto dielectric performance

02/20/2019

Name of Principal Investigators (PI): Yuanzhe Piao

- e-mail address : parkat9@snu.ac.kr
- Institution : Graduate School of Convergence Science and Technology, Seoul National University, Suwon, Korea
- Mailing Address : Graduate School of Convergence Science and Technology, Seoul National University. 145, Gwanggyo-ro, Yeongtong-gu, Suwon-si, Gyeonggi-do, 16229, Republic of Korea
- Phone : +82-31-888-9141
- Fax : +82-31-888-9148

Name of Principal Investigators (Co-PIs): Sylvie Begin-Colin

- e-mail address : Sylvie.Begin@ipcms.unistra.fr
- Institution : Institute of Physics and Chemistry of Materials, University of Strasbourg, Strasbourg, France
- Mailing Address : Institute of Physics and Chemistry of Materials, University of Strasbourg, Strasbourg, France
- Phone : +33 (0)3 88 10 71 49
- Fax : +33 (0)3 88 10 72 49

Name of Principal Investigators (Co-PIs): Peter Kofinas

- e-mail address : kofinas@umd.edu
- Institution : Fischell Department of Bioengineering, University of Maryland, College Park, Mayland, USA
- Mailing Address : 2113D Chemical and Nuclear Engineering Building, James Clark School of Engineering，University of Maryland, College Park, MD 20742，USA
- Phone : +1 301 405-7335
- Fax : +1 301-405-0523

Period of Performance: 07/31/2017 – 07/30/2018

Abstract:
Traditional magnetite nanoparticles have a saturation magnetization between 45 emu/g and 55 emu/g due to surface and volume spin canting and defects. However, it has been recently demonstrated that it is possible to improve the saturation magnetization of magnetite nanoparticles by their collective oriented organization in a single nanostructure. We synthesized corona shaped magnetite nanostructures that acquire collective assembly during synthesis. Stretchable magneto-dielectric composites were prepared using collectively assembled iron oxide nanostructures as fillers in an elastomer (polydimethylsiloxane) matrix. The resulting composites can also be stretched up to 165% strain before failure due to good adhesion between the elastomer and citrate capped RSNs. Magnetically recoverable photocatalyst was prepared by supporting TiO_2 nanoparticles on a superparamagnetic raspberry shaped nanostructures iron oxide nanocluster core@fibrous silica shell nanocomposite. In addition, by using raspberry-shaped iron oxides nanoparticles as core material, carbon nanoshell was further coated by facile methods.
We have demonstrated that raspberry shaped magnetite nanostructures are very interesting and even key elements to fabricate flexible materials with low dielectric loss, high permittivity and permeability values at radio frequencies (1 MHz- 1 GHz). The permeability values achieved by composites made

from collectively assembled corona magnetite nanoparticles are significantly higher than the existing magnetite-polymer composites and magnetite-PDMS composites. Additionally, the composites prepared with collectively assembled corona magnetite nanoparticles exhibit an extraordinary magnetic resonance, which changes with the particle size of magnetite nanoparticles. In contrast to these interesting and promising properties of the composites, the composites have high dielectric loss, which can be addressed easily by introducing an insulating layer around the magnetite nanoparticles. We believe such composites could be utilized for high-bandwidth radio frequency antennas as the dielectric loss values are further decreased.

Introduction:

Traditional magnetite nanoparticles have a saturation magnetization between 45 emu/g and 55 emu/g due to surface and volume spin canting and defects. However, it has been recently demonstrated that it is possible to improve the saturation magnetization of magnetite nanoparticles by their collective oriented organization in a single nanostructure. The research group of Pr. Sylvie Begin-Colin at IPCMS has synthesized corona shaped magnetite nanostructures that acquire collective assembly during synthesis. These nanostructures displaying a “raspberry” morphology have been synthesized by a solvo-thermal method adapted from Cheng et al. [*J. Chen et al. Adv. Mater. 17, (2005), 582-586*]. Nanostructures consist of spherical aggregates of small nanocrystals that exhibit hollow structures. The nanostructure size may be tuned in the range of 100 - 500 nm, and the nanocrystal sizes are modulated between 2 nm and 30 nm. These different nanostructures obtained by varying the reaction conditions (reaction time, reactants concentration) have been carefully characterized by different techniques such as HR-TEM, 3D tomography, SEM, BET, TGA, XRD, etc. Furthermore, the different reaction steps occurring during the synthesis have been investigated more intensively by following the temperature and pressure evolutions inside an instrumented autoclave. To produce larger amount of raspeberry shaped nanostructures (RSNs) necessary for magneto dielectric measurements, another bigger autoclave has been built and allowed producing 20h/batch. It has allowed providing the large amount of nanostructures to perform measurements at various frequencies. This synthesis part has led to a paper which should be submitted before june 2016, entitled “Formation Mechanism of Iron Oxide Raspberry Shaped Nanostructures” by Olivier Gerber, Benoit P. Pichon, Dris Ihawakrim, Ileana Florea, Simona Moldovan, Ovidiu Ersen, Dominique Begin, Jean-Marc Grenèche, Sebastien Lemonnier, Elodie Barraud, Sylvie Begin-Colin.

Two types of corona magnetite nanostructures with a mean size of 250 nm consisting of an orientated assembly of smaller magnetite nanoparticles with sizes either of 5 nm or 25 nm have been selected for the fabrication of flexible magnetodielectric composites by Professor Kofinas. First experiments have been performed with as synthesized RSNs by Prof. Peter Kofinas but the dispersion of RSNS in the polymer matrix was not optimal. Therefore other batches of RSNs have been synthesized and citrated before sending them to Pr Kofinas. These citrated nanostructures, which are monocrystalline due to an oriented aggregation induced by the synthesis process, have achieved saturation magnetization values of 74 emu/g and 88 emu/g, respectively. Another important magnetic aspect of such RSNs is their infinitesimally small coercivity. Such magnetic nanostructures with high saturation magnetization and low levels of coercivity were shown to be promising candidates for magnetic fillers to fabricate high performance flexible magnetodielectric composites. This part has led to a published paper in J. Mater. Chem. C, 2016, 4, 2345 entitled “Stretchable Magneto-dielectric Composites Based on Raspberry-Shaped Iron Oxide Nanostructures” by Mert Vural, Olivier Gerber, Benoit P. Pichon, Sebastien Lemonnier, Elodie Barraud, Leo C. Kempel, Sylvie Begin-Colin and Peter Kofinas. The research of magnetically recoverable photocatalyst prepared by supporting TiO_2 nanoparticles on RSNs core@fibrous silica shell nanocomposite has led to a published paper in RSC Advances, 2017, 7, 9587 entitled “A magnetically recoverable photocatalyst prepared by supporting TiO_2 nanoparticles on a superparamagnetic iron oxide nanocluster core@fibrous silica shell nanocomposite” by Bokyung Seo, Chaedong Lee, Donggeon Yoo, Peter Kofinas and Yuanzhe Piao.

Experiment:

Iron oxide porous nanostructures have been synthesized by a modified polyol solvothermal appro ach involving iron chloride hexahydrate, urea, ethylenglycol and succinic acid as reactants. When the reaction is performed for 13 h under solvothermal conditions in a Teflon lined autoclave at 200 °C, a black powder is obtained which is washed successively with water and ethanol. SEM micrograph showed particles featured by a spherical shape and a size distribution centered to 250

nm (Figure 1a). They consist in aggregates of nanograins of 25 nm as shown by TEM micrographs (Figure 1b). Nanostructures are mainly constituted in the magnetite phase (a= 8.39(7) Å to compare to that of stoechiometric magnetite a= 8.396 Å (magnetite JCPDS file 19-629) and 70% of magnetite from Mössbauer spectra) (Figure 1f) and are featured by similar crystal orientation. Their saturation magnetisation is about 81 emu/g, larger than that of individual 25 nm sized iron oxide NPs. Furthermore, SEM micrographs showed some cavity of about 90 nm in broken RSNs which corresponds to a hollow structure (Figure 1d). It was confirmed by studying the cross-section of these objects after their embedding in a resin followed by a polishing step (Figure 1e).

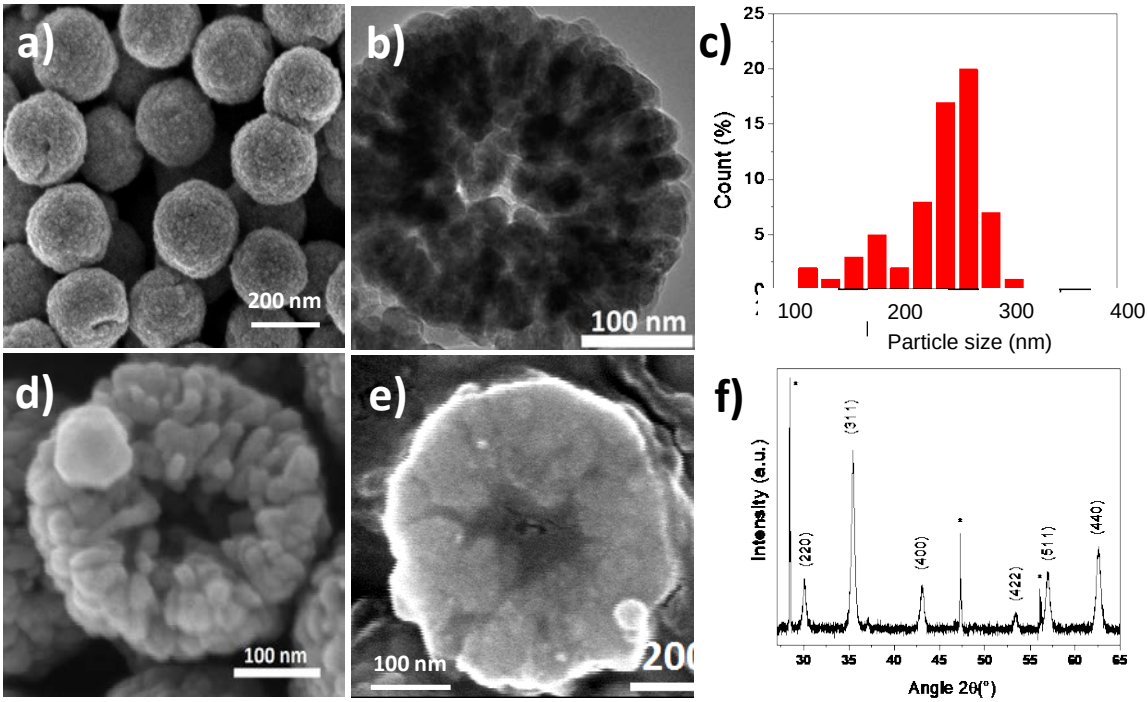

Figure 1. RSNs obtained after 13 h of reaction. a) SEM micrograph. b) TEM micrograph. c) Size distribution. SEM images on d) broken RSN and e) on the cross-section after embedding in a resin matrix and polishing. f) XRD pattern, stars correspond to silicon which used as a reference.

For a better understanding of the reaction mechanism, a time-resolved study has been performed by SEM on samples collected after different reaction times (Figure 2 and schema 1). After 4 hours of reaction, a gel-like structure with non-regular shape grains has been observed (Figure 2a), which is amorphous according to XRD analysis (not shown). FTIR spectrum exhibits Fe-O and C-H bands at 500 cm^{-1} and 2900 cm^{-1}, respectively which suggests the formation of an iron oxide based complex. After 5 h, the amorphous compound is no longer present and rather plate-like structures (PLS) with irregular morphologies (Figure 2b) and some small RSNs (with a mean size of about 100 nm) were observed (Figure S3 mais qui devient S2). After 6 h, RSNs are exclusively observed and are featured by a rather large bimodal size distribution with two main sizes centered to 90 nm and 200 nm with a heterogeneous nanograin (NG) size around 3-5 nm (Figure 2c). The mean RSN size get quite homogeneous after 7 h with a mean size of 250 nm with dispersion from 50 to 70 nm and then does not increase with reaction time. In contrast, the NG size increases gradually with the reaction time (up to 13 h). The porous structure has been also investigated by performing nitrogen absorption-desorption measurements (Table 1). Specific surface areas were estimated by the Brunauer-Emmett-Teller model and decrease gradually when reaction time increases which is in agreement with the increase in the NG sizes. After 9 hours of reaction, the formation of a cavity is observed. The increase of grain size may be correlated to the formation of cavities in RSNs since, given the experimental conditions, longer reaction times favor inside-out (or inverse) Ostwald ripening. The inner part of RSNs solubilizes and recristalizes onto grains located at the surface of RSNs. The observed synthesis pathway is described in Schema 1. To better understand the synthesis mechanisms, the PLS have been deeply investigated.

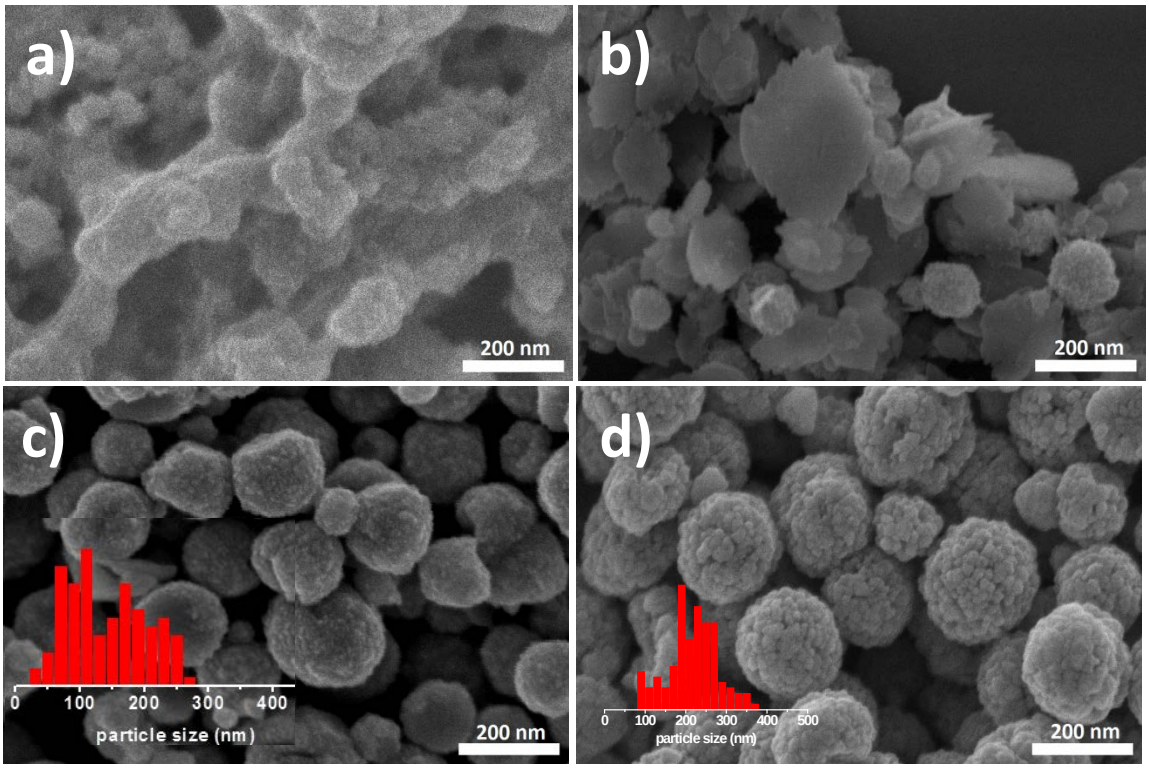

Figure 2. SEM micrographs corresponding to samples collected after a) 4 h, b) 5 h, c) 6 h and d) 9 h of reaction. Insets correspond to the size distribution measured from SEM micrographs.

Table 1. Structural caracteristics of raspberry-shaped nanostructures.

Reaction time	RSN size (nm)	Nanograin size (nm)	Surface specific area (m^2/g)
6h	90 & 200 ± 10	5 ± 3	61
7h	250 ± 50	5 ± 2	57
9h	250 ± 30	12 ± 2	38
12h	250 ± 12	25 ± 3	27

The intermediate formation of PLS is rather surprising and, to the best of our knowledge, has not been reported yet as an intermediate compounds in the synthesis of iron oxide nanocrystal clusters by the polyol solvothermal method. As they appear as key step in the synthesis process, their structure has been deeply investigated by TEM, TGA, IR and in situ TEM studies in temperature. This study is detailled in the paper to be submitted.

Results and Discussion:

(1) Formation mechanism study

The formation of RSNs is rather complex since the reaction proceeds through a multistep process (Scheme 1). The observation of the RSN synthesis at different reaction times has shown that an amorphous phase is formed after 4 hours and after 5 hours, small RSNs are observed together with PLS. When the reaction time increases, the PLS disppear simultaneously with the observation of a growth in the mean size of RSN (the NG size staying similar) which stabilizes after 7h of reaction. From 7h of reaction, the increase in the reaction time does not modify the mean size of RSNs while the mean size of NG increases and a core cavity forms.

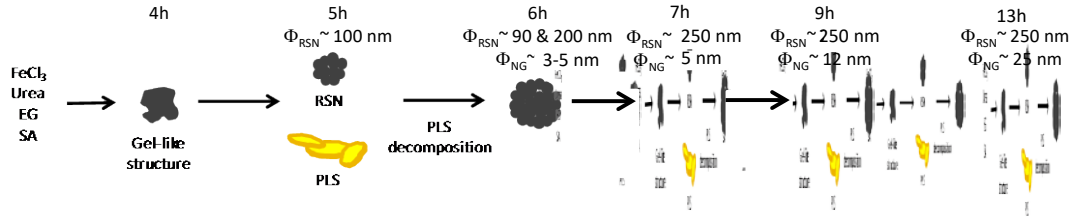

Schema 1. Schematic representation of the synthesis pathway.

The temperature and pressure have been recorded during the synthesis (Figure 3) in order to get a better understanding on the reaction mechanism. One may first notice that after 4h hours of rea ction, the temperature and pressure are stabilized and the observed phases are thus formed in sim ilar conditions of pressure and temperatures. An increase of pressure is observed after 2,5 h and is directly correlated to the endothermic peak at 130 °C in the temperature curve. These features correspond to the decomposition of urea in ammoniac which is catalyzed by hexahydrate Fe(III) chlorides. Indeed they are not observed when heating the reaction medium without using $FeCl_3$.6 H_2O (Figure 3). Then ammonia reacts with water molecules leading to the formation of OH^- + N H_4^+. These conditions (increases the alkalanity of the reaction media and presence of hydroxides) are well known to favor the co-precipitation of iron oxide NGs from intermediate iron hydroxid es. That would explain the observation of small RSNs after 5 h of reaction.
However an amorphous phase is observed before at 4h and may be due to competitive interactio ns. Indeed when urea decomposes in ammoniac, alkaline conditions favor also the deprotonation of ethylene glycol which coordinate with Fe species. Therefore one may suggest that the amorph ous phase observed after 4 h of reaction results from the competitive interaction of ammonia wit h water and EG leading thus to amorphous intermediate alkoxide and iron hydroxyde phases.
After 4 hours, the temperature and pressure reach their maximum and favor the formation of plat e-like structures resulting from interaction of iron cations with OH- and deprotonated ethylen gly col and the coprecipitation of smal iron oxide NGs. The reaction conditions favor the agregation of these NGs in nanostructures. The thermal studies performed on PLS have shown that these PL S are thermallly stable at high temperature which explains that they are identified and also may be easily extracted from the reaction media after 4 h of reaction. Besides some PLS may be sho wn to be incorporated in RSNs. However at 4 h, the maximum temperature and pressure are rea ched and the PLS begin to decomposes. PLS acts as an intermediate iron precursor (or iron reser voir) which decomposes at higher temperature and should induce heterogeneous nucleation of na nocrystals on previously formed iron oxide based RSNs. This would explain the increase of the mean RSNs size when that of NGs stays quite constant between 4 and 7 hours of reaction.

Such heterogeneous nucleation should favor the oriented agregation of NGs which is em phasized by the high pressure and temperature conditions which lead to well-shaped RSNs with narrow size distribution after 7 h of reaction. From 7h, there are no more iron precursors availab le in the media and RSNs reach their maximum sizes. As the reaction time increases in these hi gh pressure and temperature conditions, digestive inside-out Ostwald ripening proceeds to solubili zation-recrystallization of grains. Nanograins located at the center of RSNs undergo solubilization while the ones located close to the surface grow with the reaction time.

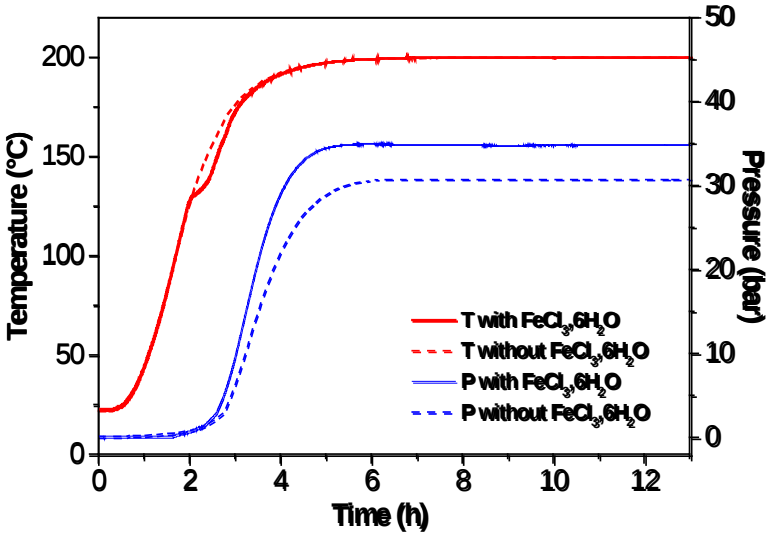

Figure 3. Temperature and pressure measurements as function of reaction time with (solid line) a nd without (dot line) iron chloride precursor.

(2) Design and structural and magnetic characterizations of citrated raspberry nanostructures for the fabrication of stretchable magneto-dielectric composites.

The iron oxide RSNs have been synthesized by a one-pot modified polyol solvothermal method. The reaction time may be used to alter the structure, composition and magnetic properties of the filler iron oxide RSNs (see § above). The solvothermal syntheses with reaction periods of 7 and 13 hours, result in spherical hollow clusters with a similar mean size around 250 nm and constituted of iron oxide nanocrystals with a mean nanocrystal size of 5 and 25 nm, respectively. These two types of RSNs have been selected for the fabrication of stretchable magneto-dielectric composites. However to favor their dispersion in polymer matrix, these RSNs have been citrated and their characterization is detailled below.

The structure of the RSNs fillers prepared using two reaction durations was characterized with X-Ray diffraction, Mössbauer spectroscopy and electron microscopies. The scanning electron microscopy (SEM) images revealed that both RSN fillers have an average diameter of about 250 nm (Figure 4 a, d). The surface roughness apparent in SEM images is indicative of a c luster-like structure. The transmission electron microscopy (TEM) characterization has demonstr ated that these nanoclusters possess a hollow core, which validates the raspberry-like shape of this filler material (Figure 4a-inset, d, e). High-resolution TEM (HRTEM) images of the inter face between two crystals in these RSN filler materials (Figure 5) and selected area electron diffraction (SAED) patterns (Figure 4c, f) confirm the oriented attachment of nanocrystals in RSNs. Indeed the HRTEM images clearly demonstrate that crystallographic orientations of nan ocrystals are matched at the interface, which is indicative of a common crystal orientation sha red by nanocrystals forming the RSN fillers (Figure 5). SAED patterns verified the formation of the spinel phase (Figure 4 c, e) and are consistent with single crystal structures (SAED pa tterns on single RSNs show Von Laue patterns instead of Debye rings). These observations sh ow that RSNs are constituted of aggregated nanocrystals, which have similar crystallographic orientations.

The detailed characterization of the RSNs microstructure has showed that RSN fillers allowed to react for 7 hours (RSN5) have finer nanocrystal size than fillers allowed to react for 13 hours (RSN25) (Figure 4). From TEM micrographs, a mean nanocrystal size of 5 and 25 nm is determined for RSN5 and RSN25 respectively while crystallite sizes calculated from Rietv

eld analysis of X-Ray Diffraction (XRD) patterns (Figure 5b) are respectively 14 ± 1 and 15 ± 1 nm. Such discrepancies between both measurements were related to the monocrystalline nature of the RSNs and the presence of defects or dislocation induced during the synthesis pr ocess. Indeed SAED patterns (Figure 4.c,f) and HRTEM of nanocrystal interfaces (Figure 5a) confirms the monocrystalline structure of RSNs, which is established with aggregates of nanoc rystals with similar crystal orientations. However, the extended Von Laue spots in SAED patte rns evidenced a slight misalignment in the orientation of these nanocrystals. In addition, Fast Fourier Transform (FFT) analysis performed on SAED patterns of RSNs has demonstrated the presence of defects.

XRD patterns of RSNs display characteristic peaks of the iron oxide spinel structure (Figure 5b). Lattice parameter deduced from XRD pattern is very close to that of stoichiometric magn etite for RSN25 and indicates an oxidized state for RSN5. In addition, Mössbauer spectroscop y confirmed that RSN fillers with smaller crystal size have a maghemite-rich composition ($Fe_{2.78}O_4$, 70% of maghemite) while those with large crystal size are mainly constituted of magneti te Fe_3O_4 phase ($Fe_{2.90}O_4$, 70% of magnetite). These variations in composition is explained by the surface oxidation of magnetite, which might be elevated due to smaller crystal size of ma ghemite-rich RSN fillers.

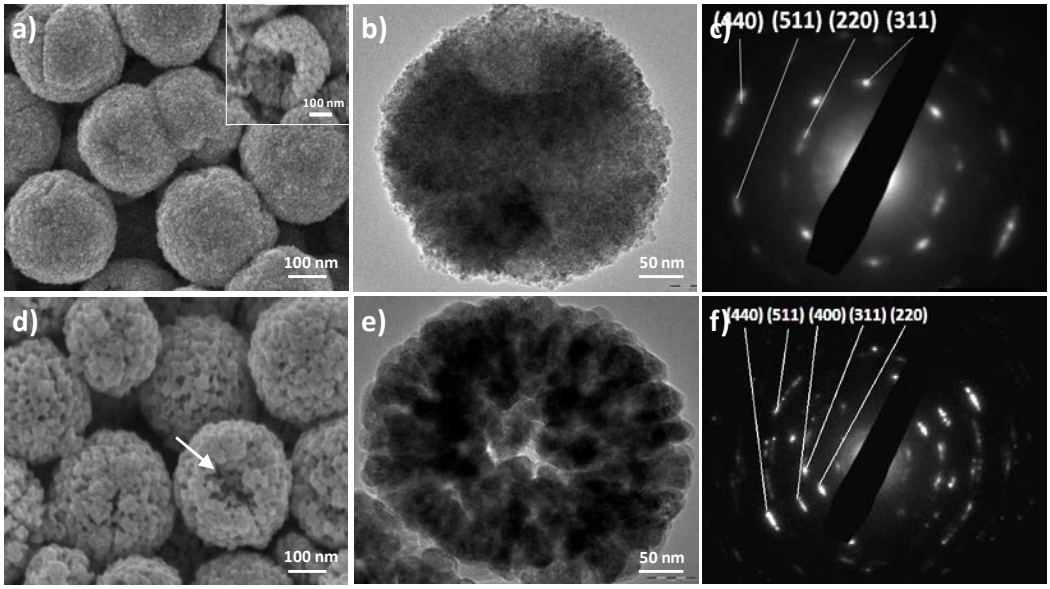

Figure 4. SEM images of citrate-capped RSNs reacted for (a) 7 hours, and (b) 13 hours. TE M images of citrate-capped RSNs reacted for (d) 7 hours, and (e) 13 hours. SAED patterns o f citrate-capped RSNs reacted for (c) 7 hours, and (f) 13 hours.

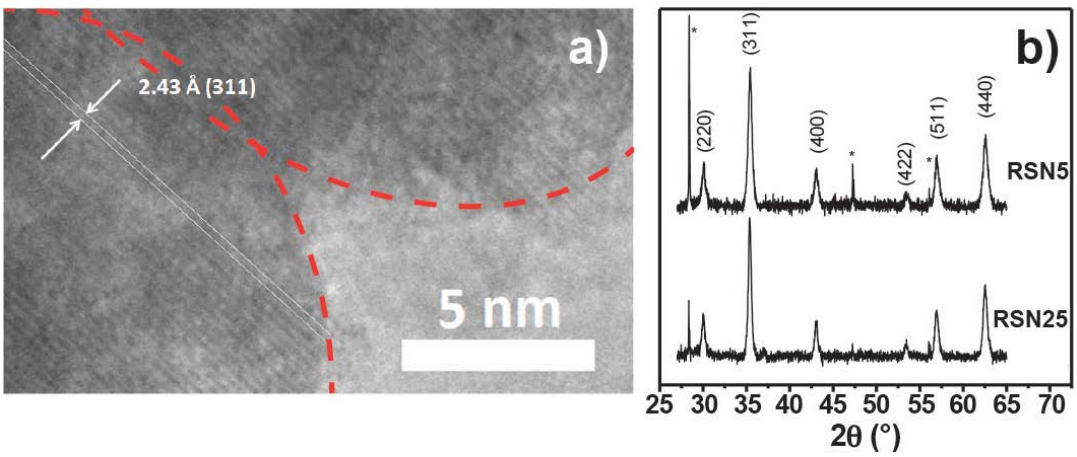

Figure 5. (a) HRTEM image of RSNs which shows on the nanostructure border that several nanocrystals display the same crystalline orientation. (b) XRD data for RSN5 and RSN25.

The characterization of the magnetic properties of RSN fillers correlates well with their structure and composition. The RSNs are superparamagnetic at 300K as the coercivity of both magnetite- and maghemite-rich RSNs at 5K remains below 300 Oe (Figure 6-insets), which is indicative of small nanocrystal size. The citrated RSN25 have demonstrated a M_s of 88 emu/g, which is comparable to the bulk M_s of magnetite (92 emu/g) and that of RSN5 is around 74 emu/g which is closed to bulk maghemite (Figure 6a,b). In contrast to RSNs, individual magnetite nanoparticles with a similar nanocrystal size have a saturation magnetization between 45 emu/g and 70 emu/g due to defects, surface and volume spin canting. In fact, the structuration of RSNs, which display aggregated orientation of nanocrystals has a critical role for improving the structural and magnetic order, limiting the influence of surface and volume spin canting. The strong dipolar interactions between nanocrystals forming RSNs favors the coupling of spins at the grain surface, which reduces the magnetic and structural disorder arising commonly from defects or broken bonds in the surface of iron oxide nanocrystals. Because of the strong dipolar interactions between nanocrystals, and the common crystallographic orientation of grains, RSNs exhibit higher crystal quality, and lower spin canting than individual iron oxide nanoparticles, which leads to magnetization values matching bulk materials.

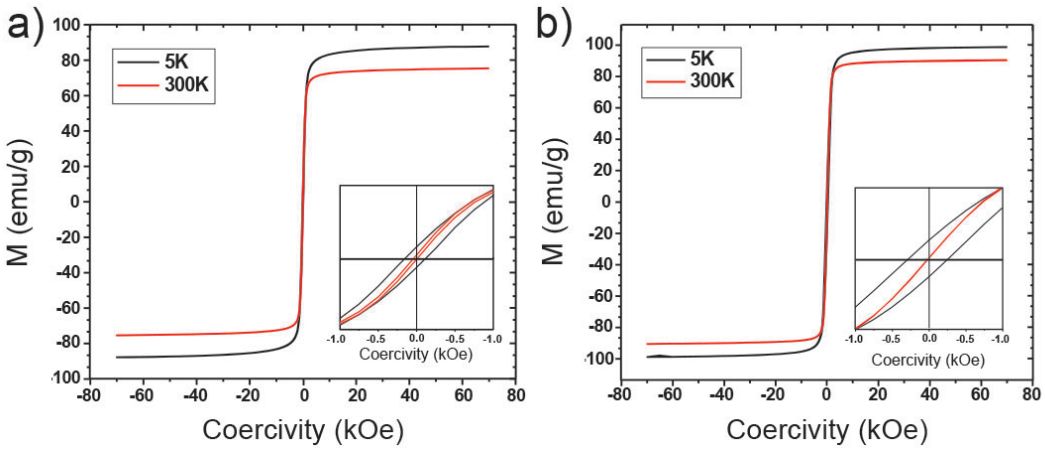

Figure 6. Magnetization curves for a) maghemite-rich (RSN5) and b) magnetite-rich (RSN25) RSNs at 5 K and 300K.

The influence of citrate capping on the surface charge of the RSNs was quantified using zeta potential experiments. The RSNs exhibited zeta potential values close to zero prior to attachment of the citrate capping agent, which is in agreement with the isoelectric point of iron oxide (IEP=6.8). The zeta potential of RSNs reached -56 mV with citrate capping, which results in better colloidal stability with the help of electrostatic interactions. These citrate-capped RSNs with a negative surface charge were easily dispersed in a polydimethylsiloxane (PDMS) elastomer matrix and cross-linked to form stretchable magneto-dielectric composites.

(3) **Magnetically recoverable photocatalyst prepared by supporting TiO_2 nanoparticles on a superparamagnetic raspberry shaped nanostructures iron oxide nanocluster core@fibrous silica shell nanocomposite**

A magnetically recoverable photocatalyst was prepared by supporting TiO_2 nanoparticles on a superparamagnetic iron oxide nanocluster (SION) core@fibrous silica shell (FSS) nanocomposite. Using the raspberry-shaped magnetic iron oxide nanocluster core as a seed, FSS with uniform thickness was grown directly on the core surface by a sol-gel process. The preparation method was optimized to have a single core for each nanoparticle by adjusting the amount of the silica source. The FSS has a fanning structure of radial pores, which enable large amounts of TiO_2 nanoparticles to be supported easily on the pore surface. SION@FSS with amorphous TiO_2 loaded on the pores (SION@FSS@Am- TiO_2) was crystallized to the anatase phase (SION@FSS@A- TiO_2), which shows good photocatalytic effect. When used for water purification, SION@FSS@A- TiO_2 shows faster dye degradation kinetics than that of commercial P25 nanoparticles. The as-prepared SION@FSS@A-TiO_2 photocatalyst could be magnetically recovered easily from water after decolorization of dye.

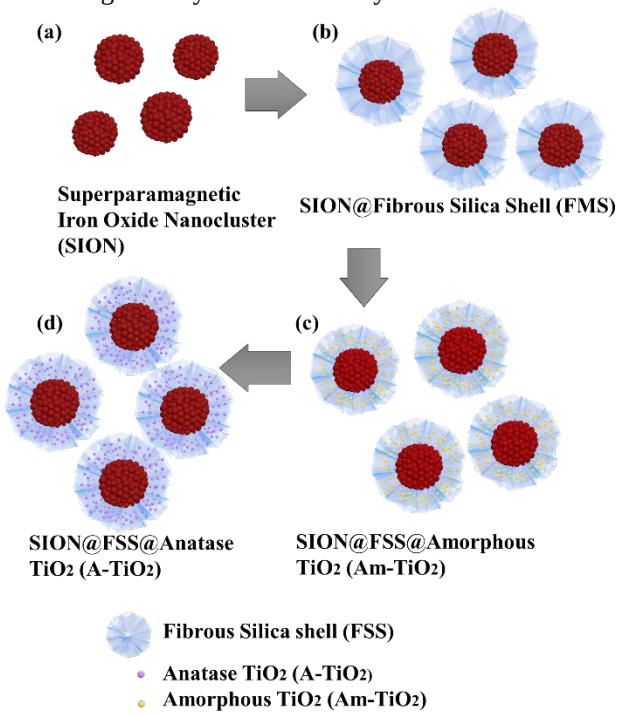

Scheme 1 Schematic of the procedure for preparing magnetically recoverable photocatalyst: (a) SION, (b) SION@FSS, (c) SION@FSS@Am-TiO_2 and (d) SION@FSS@A-TiO_2.

The procedure for the synthesis of SION@FSS@A- TiO_2 (**Scheme 1**) involves three steps. First, the SIONs are homogeneously coated with dendritic FSS by a sol-gel process. Next, amorphous TiO_2 nanoparticles were deposited on the FSS to form SION@FSS@Am-TiO_2, which undergo a hydrothermal reaction to yield the SION@FSS@A-TiO_2.

The starting SION has a raspberry-like shape4s, which is a conglobulation of 5–10-nm iron oxide nanocrystals packed into a 280 ± 37-nm nanoclusters. These SIONs combine the advantages of individual grains and confer an enhanced magnetic property. The oil−water biphase stratification approach[31] was used to prepare a silica coating shell with fibrous large pores that enable enhanced adsorption and release ability. To generate such silica coating shells, SIONs were first dispersed in water and mixed with CTAB and TEA. Then, TEOS and 1-octadecene were added to the mixture; the mixture was hydrolyzed and condensed to generate the first FSS layer on SION. The second-layer generation step starts with discarding

the oil layer and adding TEOS and decalin. The final layer is generated using a mixture of TEOS and cyclohexane as an oil-based solvent. After removing residual CTABs by calcination, TBOT was added dropwise to an ethanolic solution of SION@FSS and water. Amorphous TiO_2 nanoparticles supported on SION@FSS were crystallized using the hydrothermal method. EDX analysis shows that iron and oxide spectra are dominant in the center of the particles and silica and titanium spectra dominate on the outer side of the particles.

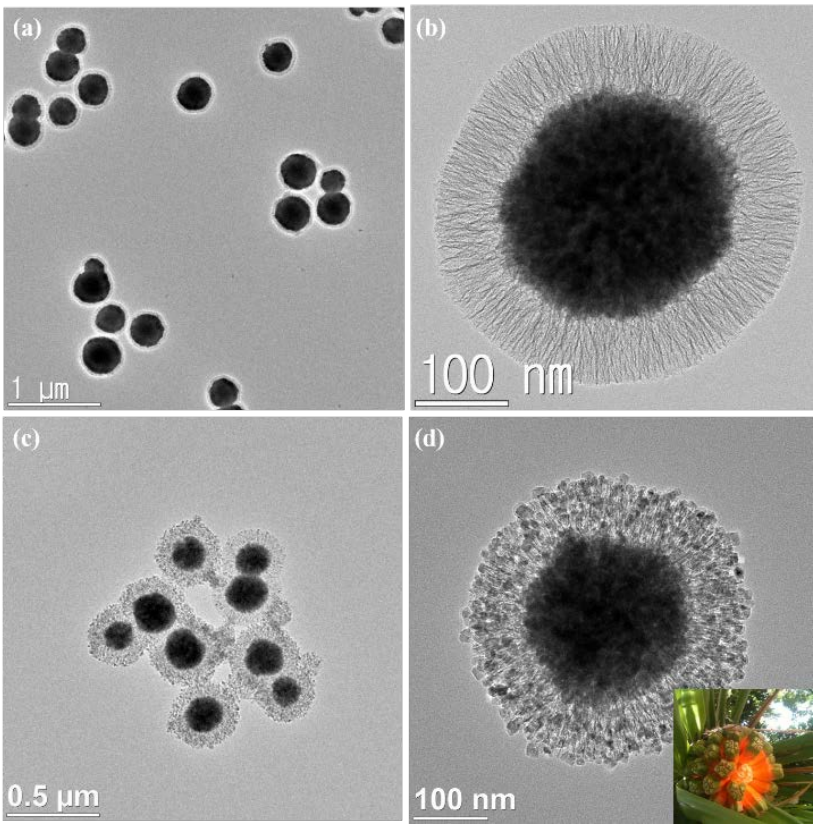

Figure 7. TEM images of SION@FSS at the end of the third layer growth (a, b) and SION@FSS@A-TiO_2 as a final product for water purification (c, d). Inset of (d) shows the picture of a screwpine which has a shape similar to that of SION@FSS@A-TiO_2

Fibrous silica shell with uniform layer thickness could be clearly seen in both TEM (**Figure 7**) and SEM images (**Figure 8**). Average size of SION@FSS was 317.7 ± 56.2 nm, as shown in the SEM images. The average layer thickness of SION@FSS was 71.1 ± 7.5 nm. SION@FSS shows wide size distribution owing to the polydispersity of the iron oxide cores, but the thickness of FSS is uniform irrespective of the size of the core. The size of prehydrothermal SION@FSS@Am-TiO_2 was 324 ± 50.0 nm and that of posthydrothermal SION@FSS@A-TiO_2 was 305 ± 37.9 nm, as derived from the SEM observations. The thickness of the coating FSS + Am-TiO_2 layer was 70.5 ± 9.1 nm. To crystalize the TiO_2 nanoparticle from amorphous to anatase phase, hydrothermal method is used due to low energy required compared to high temperature furnace method. After the posthydrothermal treatment, the layer shrunk a little to 68.9 ± 8.3 nm. It has been reported that silica could be partially etched during the hydrothermal treatment.

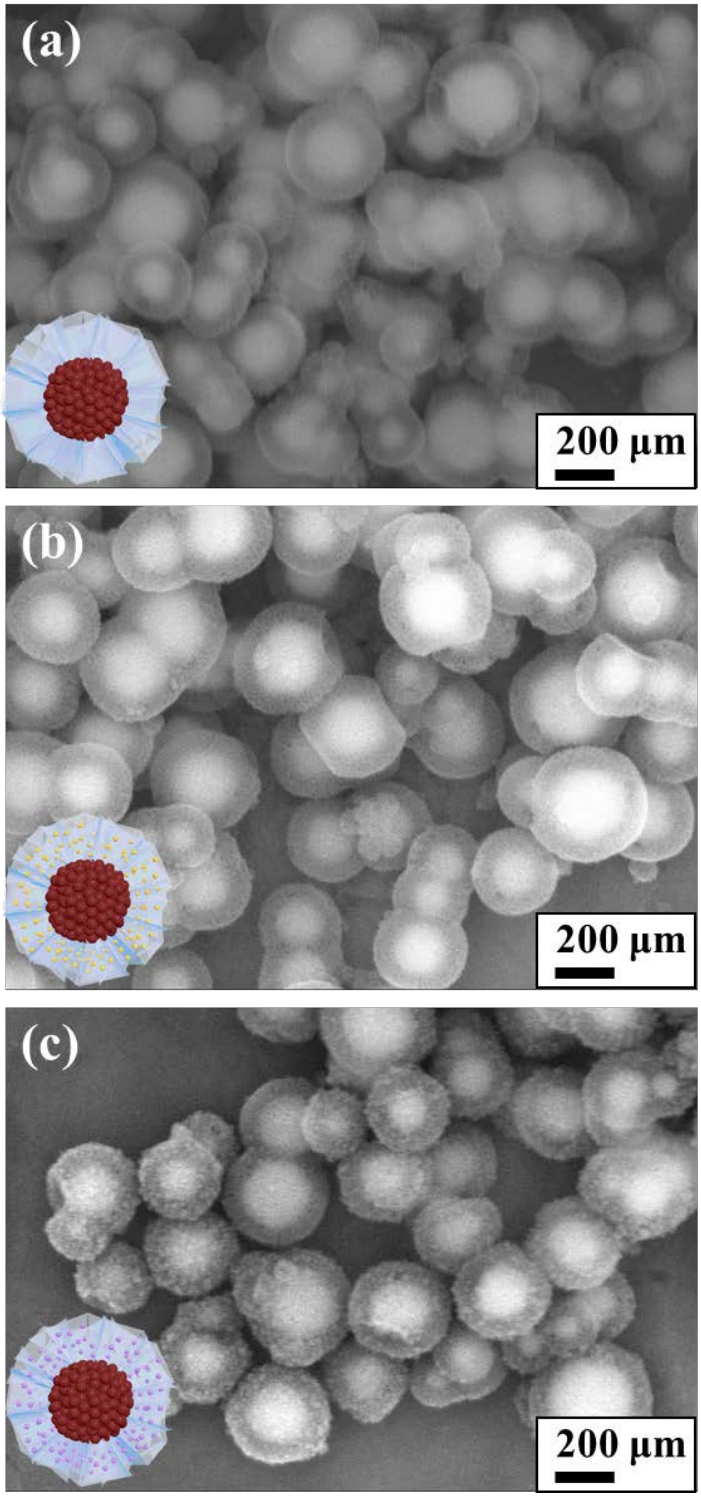

Figure 8. SEM images of (a) SION@FSS, (b) SION@FSS@Am-TiO_2 and (c) SION@FSS@A-TiO_2.

For SION@FSS synthesis without residual FSS particles, the amount of TEOS was adjusted from 4 ml to 12.5 µl during the first layer stratification. When 4 ml of TEOS was added, SION@FSS spheres were fused with several FSS particles. The aggregated FSS spheres were separated when the TEOS amount was reduced to 1 ml, but SION@FSS agglomerates were still present. Separation of fused SION@FSS was obtained by gradually reducing the TEOS volume to 250 µl. Fully separated SION@FSS nanoparticles started to appear on using 50 µl

of TEOS. By reducing the TEOS volume below 50 µl, the FSS layer becomes thinner and cannot be observed by TEM. After first and second FSS were coated on single SION@FSS nanoparticles, TEOS volume was controlled for the third layer generation. Likewise, the amount of TEOS is optimized to have single core for each nanocomposites.

To take advantage of their wide surface area and application in photocatalysis, TiO_2 spheres were confined in pores. To increase the filling amount without remnant TiO_2 spheres, the amount of TBOT was adjusted from 10 µl to 2 ml. Experimental results showed that 400–800 µl of TBOT was sufficient to fill in the FSS pores. When the TBOT concentration reached 1% (v/v), fused $SION@FSS@Am-TiO_2$ nanoparticles were observed. Otherwise, when TBOT concentration was too low, considerable number of the FSS pores remained empty. As a result, $SION@FSS@Am-TiO_2$ synthesized with 800 µl of the titanium precursor was used for further analysis.

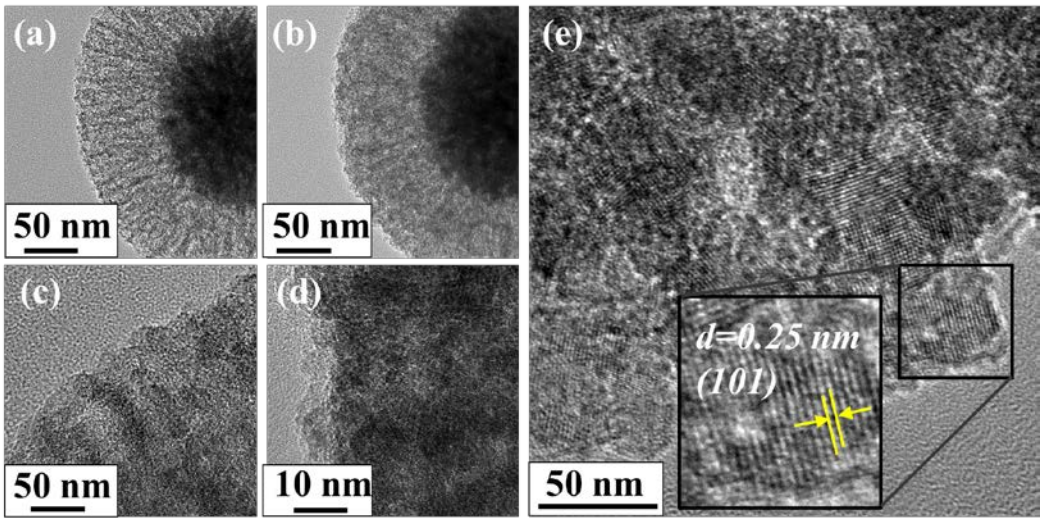

Figure 9. TEM images of IO@FSS@Am-TiO_2 showing Amorphous (a-d) to anatase phase transition of grafted titanium oxide nanoparticles. Lattice fringes correspond to (101) plane of anatase are found on IO@FSS@Am-TiO_2 (e). Amount of the TiO_2 precursor (TBOT) were adjusted to 400 µl ((a), (c) (magnified view)) and 800 µl ((b), (d) (magnified view)).

Titanium dioxide nanoparticle loading were verified from both TEM images (**Figure** 9) and EDX analysis. When 400 µl of TBOT was used (**Figure 9**, (a)), more pore voids between the FSS layers were observed compared to when 800 µl of TBOT was used (b). On magnified view (b, d), more TiO_2 nanoparticles were observed when 400 µl of TBOT was used (c) compared with that when 800 µl of TBOT (d). It shows high possibility of greater TiO_2 nanoparticles loading on SION@FSS@Am-TiO_2 by increasing the amount of titanium precursor. Loading of TiO_2 nanoparticles after hydrothermal reaction was determined by the crystalline structure the grains observed between the FSS layers, which matches the (101) plane of the anatase nanocrystals (e).

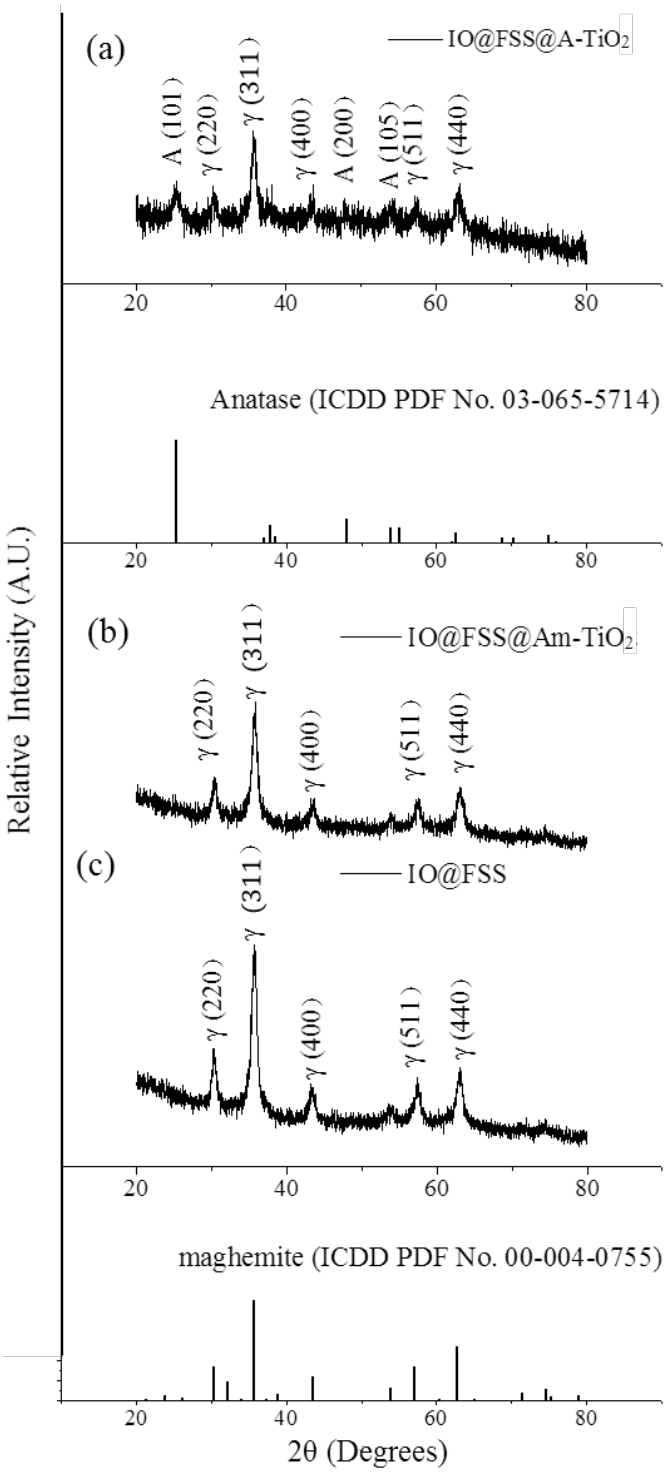

Figure 10. X-ray diffraction analysis of (a) SION@FSS@A-TiO_2, (b) SION@FSS@Am-TiO_2 and (c) SION@FSS. Crystal planes are indexed with γ (maghemite) and A (anatase).

Crystalline structures were investigated by powder X-ray diffraction (XRD) (**Figure 10**). The grain size of SION was calculated by the Debye-Scherrer equation. Using the most intense diffraction peak from figure 4 (c), the (311) plane of maghemite, it was found that the SION has 10.94 nm grains. Since amorphous TiO_2 shows less photocatalytic activity compared to anatase TiO_2, the nanocomposite undergoes crystallization. The phases of the titanium-coated

samples before and after the crystallization step were characterized (**Figure 10**). Prehydrothermal TiO_2 nanoparticles were amorphous as no $SION@FSS@Am\text{-}TiO_2$ spectrum (b) matched that of anatase (ICDD PDF card 03-065-5714). Maghemite (ICDD PDF card 00-004-0755) peaks or patterns are dominant in both XRD (**Figure 10**) and SAED (**Figure 11**) results, suggesting that the iron oxide core is maghemite in nature with polycrystalline structure. The core is initially magnetite, but undergoes transition to maghemite during the hydrothermal reaction. After the hydrothermal reaction, the diffraction spectrum obtained from $SION@FSS@A\text{-}TiO_2$ (**Figure 10** (a)) shows a peak at 25.3˚ corresponding to the (101) reflection of anatase. Peaks at 48.04˚ and 53.88˚ are attributed to the (200) and (105) planes, respectively, of the anatase-phase TiO_2.

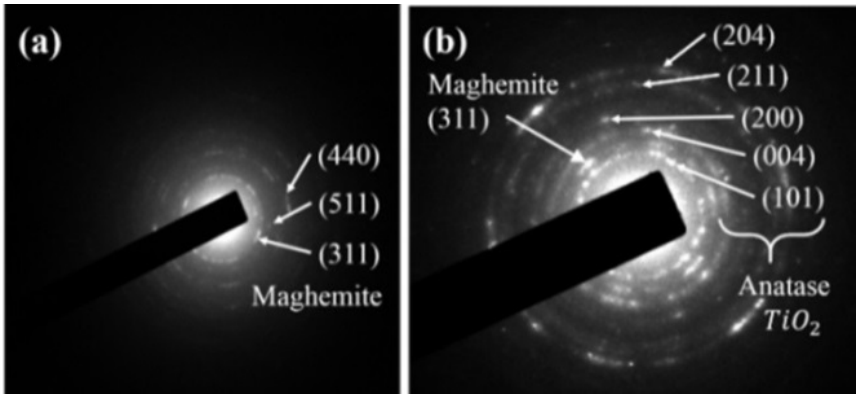

Figure 11. SAED patterns of (a) SION@FSS@Am-TiO_2 and (b) SION@FSS@A-TiO_2.

Although maghemite spectra are dominant in XRD, SAED analysis clearly revealed the existence of other anatase planes. The five ring patterns in (**Figure 11,** (b)) correspond to the (204), (211), (200), (004), and (101) planes of anatase TiO_2. The most intense peak of $SION@FSS@A\text{-}TiO_2$ in the SAED patterns corresponds to the (311) plane of maghemite. To sum up, appearance of anatase peaks prove the transition of amorphous to anatase phase of the supported TiO_2 after the hydrothermal treatment.

Table 1 Morphological and textural characteristics of the nanoparticles

Sample Name	S_{BET} (m^2/g)	V_t (cm^3/g)	D_{BIH} (nm)
SION@FSS	265.62	0.745	11.22
$SION@FSS@Am\text{-}TiO_2$	237.07	0.434	8.39
$SION@FSS@A\text{-}TiO_2$	149.98	0.434	12.77

S_{BET}, Brunauer-Emmett-Teller pore surface area (m^2/g). V_t, Single-point adsorption total pore volume at P/P_o=0.994; D_{BIH}, Barrett-Joyner-Halenda adsorption average pore diameter.

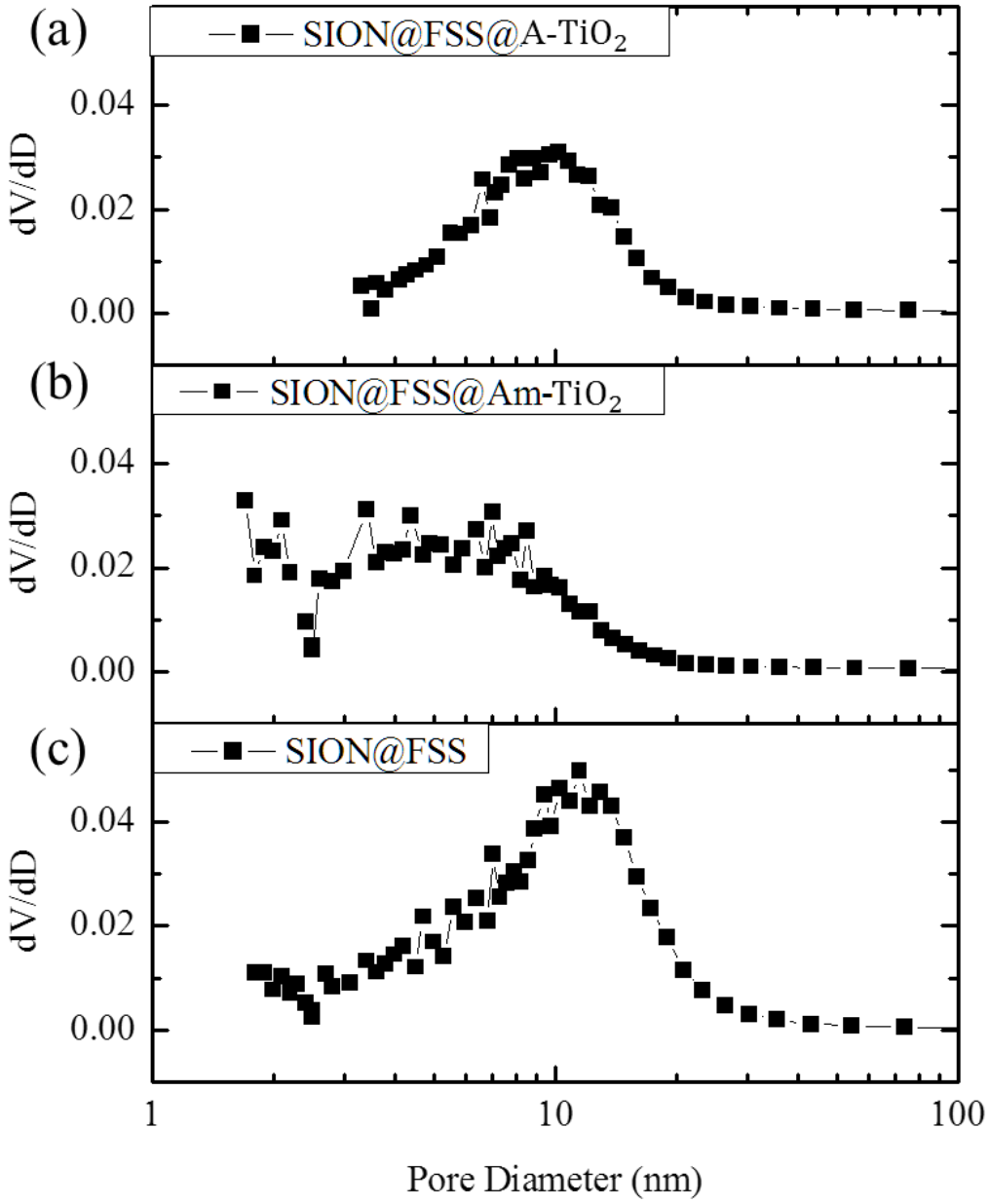

Figure 12. Pore size distributions of SION@FSS (a), SION@FSS@Am-TiO_2 (b) and SION@FSS@A-TiO_2 (c).

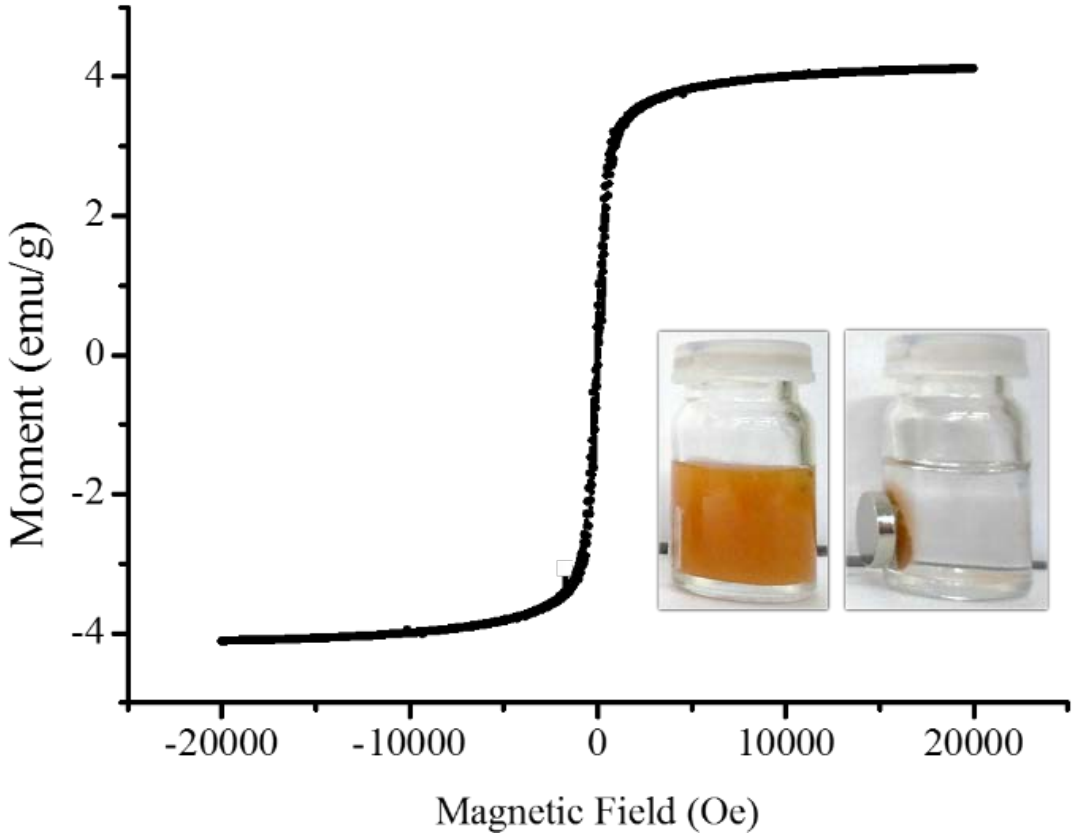

Figure 13. Field-dependence of magnetization graph of SION@FSS@A-TiO_2 measured at 20 K. Inset shows SION@FSS@A-TiO_2 dispersed in ethanol (left) and magnetically collected SION@FSS@A-TiO_2 (right).

Morphological change at each synthesis step is summarized in the **Table 1**. Total pore volume of the SION@FSS spheres, 0.745 cm^3/g, match that of the FSS spheres from the previous report, 0.689 cm^3/g. Reduced surface area of SION@FSS@Am-TiO_2 confirms that TiO_2 is supported in the SION@FSS pores. During the hydrothermal reaction, amorphous TiO_2 undergoes crystallization and crystal growth, leading to the increased TiO_2 nanoparticle size. Thus, pores below 10 nm are absent from the pore size distribution graph of SION@FSS@A-TiO_2 (**Figure 12**). Therefore, increased pore size after hydrothermal reaction is expected to be due to the removal of micropores and mesopores from between the TiO_2 nanoparticles. This also leads to close packing of the TiO_2 nanoparticles, which reduces the SION@FSS@A-TiO_2 surface area to 149.98 m^2/g.

The nanoparticles were recollected using the magnetic property of the iron oxide core. The graph of induced magnetization versus field shows saturation magnetization at 4.114 emu/g (**Figure 13**). Saturation magnetization of SION@FSS@Am-TiO_2 is lower than that of the iron oxide core, owing to the presence of silica and TiO_2 nanoparticle that do not contribute to magnetic induction. In addition, the combined effect may be integrated with the reduced magnetization value. Surfactants on SION cores may act as a carbon source and become amorphous carbon during the annealing of SION@FSS so does magnetization value may slightly enhanced. Due to the thickness of the shell, magnetic moment may change. All the nanoparticles that were synthesized based on SION@FSS were dragged by a small handheld magnet and were redispersed easily by shaking the vials after withdrawing the magnet.

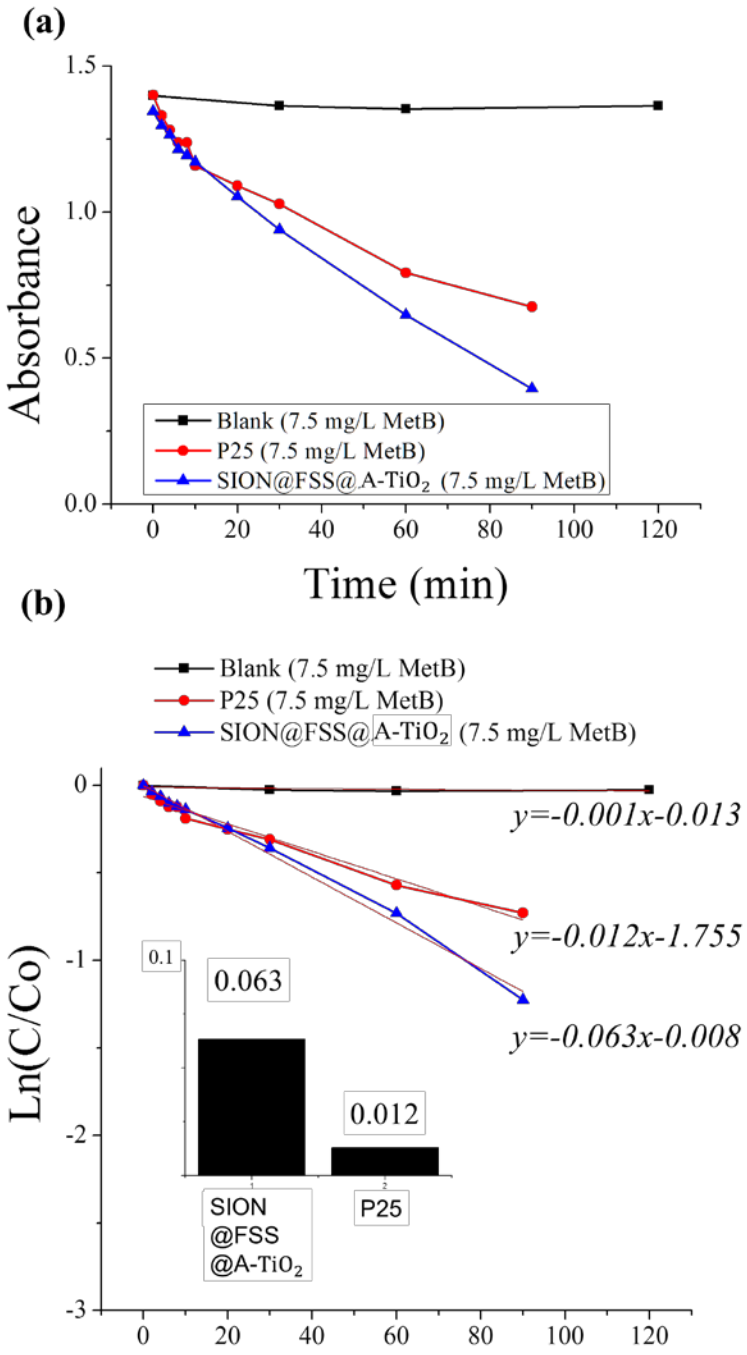

Figure 14. Degradation test with MetB solution (7.5 mg/L) and SION@FSS@A-TiO_2 compared to that with commercial P25. Absorbance vs. time (a) data was linear fitted (b) to compare rate constants (inset).

Finally, the catalytic effect of the anatase TiO_2 decorated on the particle surface is evaluated (Figure 14), after reaching the absorption-desorption equilibrium after 2hr. MetB solution was purified using UV-illuminated catalyst nanoparticles, SION@FSS@A-TiO_2. With the aid of SION@FSS@A-TiO_2, 3 mg/L of dye molecules were degraded before 3 h of UV-irradiation. SION@FSS@A-TiO_2 shows much higher dye decomposition rate than same amount of commercial P25 TiO_2 nanoparticles (Figure 14 (b), (c)). Since a considerable amount of non-catalytic materials are included in the mass of SION@FSS@A-TiO_2, rate constant in Figure 14 might be higher for the reaction with catalysts, SION@FSS@A-TiO_2. Considering

the very low first-order rate constant of anatase TiO_2 nanoparticles and thin film made in a similar manner without magnetic core and silica supports, the synthesis and the use of SION@FSS@A- TiO_2 may enhance the photocatalytic effect. Finally, the nanoparticles were reused after the degradation. The recycled SION@FSS@A-TiO_2 shows less catalyst deterioration after the repeated trials while retaining its structure at the end of the degradation trials. The removal time and concentration of degraded MetB dye is compared with other magnetically recollectable nanocomposites with TiO_2 nanoparticles. From the results, SION@FSS@A-TiO_2 show comparable degradation performance while considering the lamp intensity and amount of catalysts used.

(4) By using raspberry-shaped iron oxides nanoparticles as core material (by Prof. Sylvie Bégin-Colin's group), carbon nanoshell is coated by two methods (by Prof. Yuanzhe Piao's group).

(4-1) Carbon nanoshell coating (Method 1)

Raspberry-shaped iron oxides nanoparticles (RSN) are mixed with iron oleate (RSN : iron oleate = 1 : 2 in weight) and heated at 600 °C under Ar gas. It is confirmed that there is no aggregation or shape change during carbon coating.

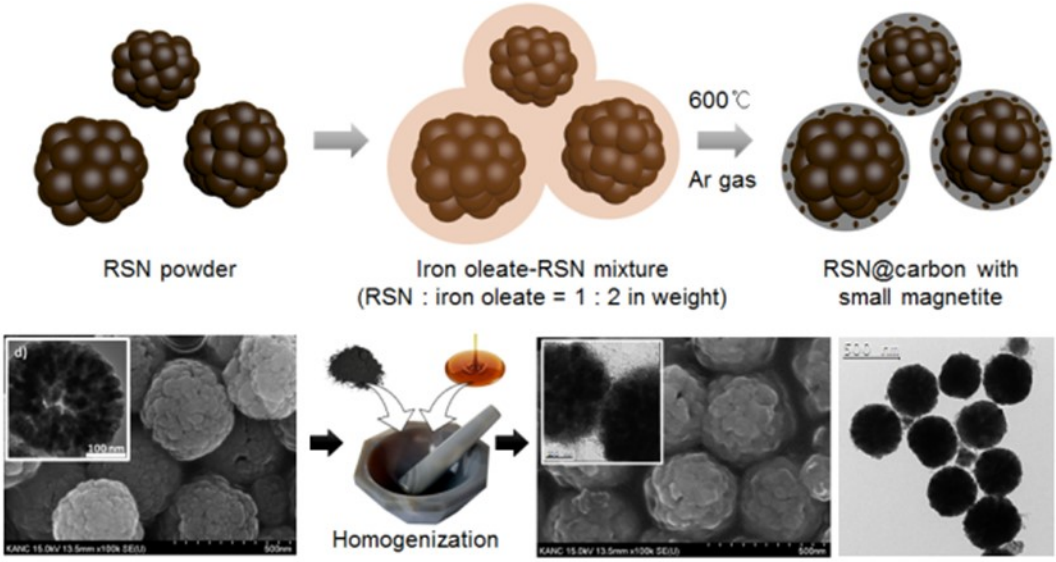

Figure 15: Carbon nanoshell coating Method 1. RSN are mixed with iron oleate (RSN : iron oleate = 1 : 2 in weight) and heated at 600 °C under Ar gas.

(4-2) Carbon nanoshell coating (Method 2)

Carbon nanoshell coated RSN is obtained via microwave irradiation of polydopamine-coated RSN. Normal heat treatment process for carbonization is usually time-consuming. In our work, microwave irradiation is used to carbonization. Since magnetic particles absorb microwave and produce heat, we successfully convert polydopamine-coated RSN to carbon coated RSN within seconds. The method is simple, fast and universal.

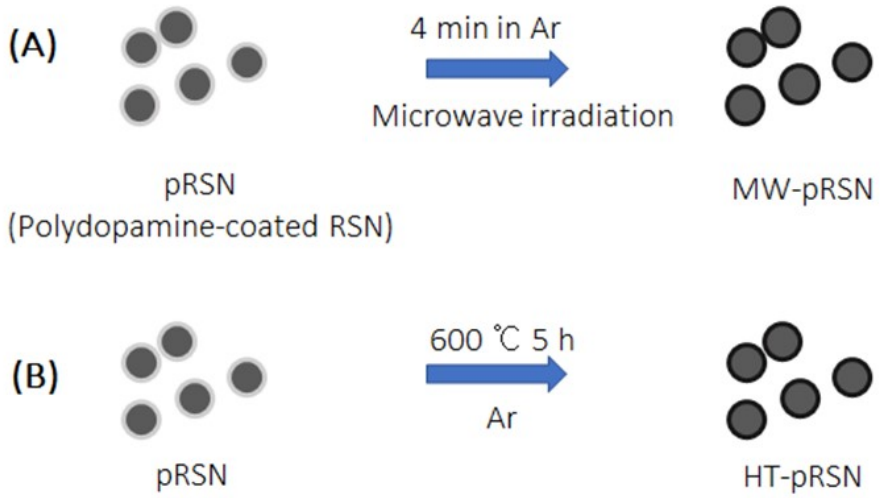

Figure 16: Method 2. (A) Ultrafast synthesis of carbon-coated magnetic particles via microwave irradiation MW-pRSN), (B) Normal heat treatment to convert polydopamine-coated RSN to carbon coated RSN (HT-pRSN).

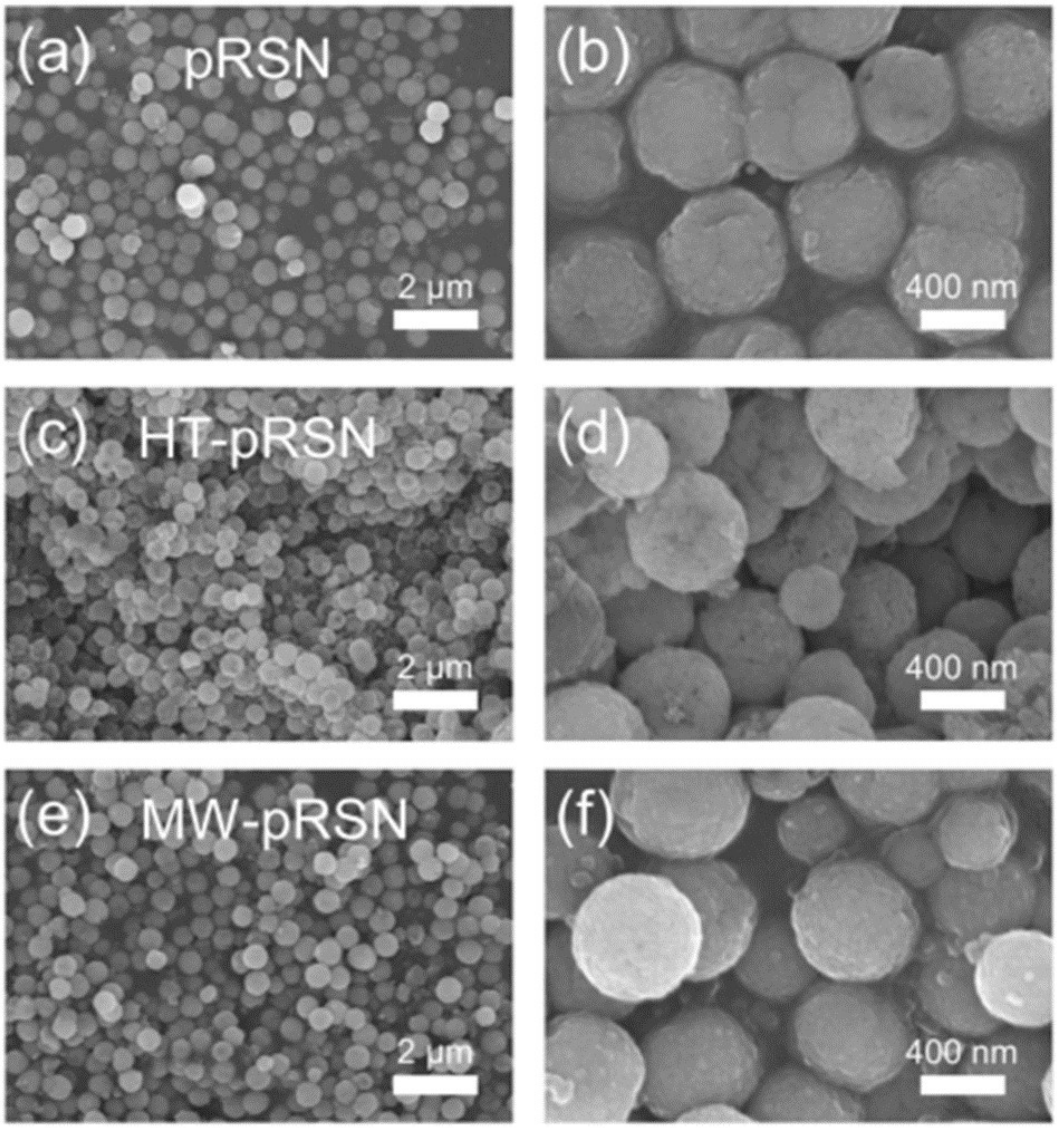

Figure 17: SEM images of pRSN, HT-pRSN and MW-pRSN.

These materials will be embedded in polymer matrix and tested by Prof. Peter Kofinas's group for magneto dielectric properties.

(5) Prof. Sylvie Bégin-Colin's group is working on the RSN synthesis and doping

(5-1) Size modification of RSN and of grains in RSN to enhance collective magnetic properties

Water and reaction time are important factors to tune the morphology of RSN. The hydration rate of the starting iron chloride III precursor was found important for the size of RSNs, and reaction and cooling times for the size of grains constituting the RSN.

Typical solvothermal synthesis of RSN showing the tuning of RSN's size by tuning the iron chloride III lots (**Figure 18**).

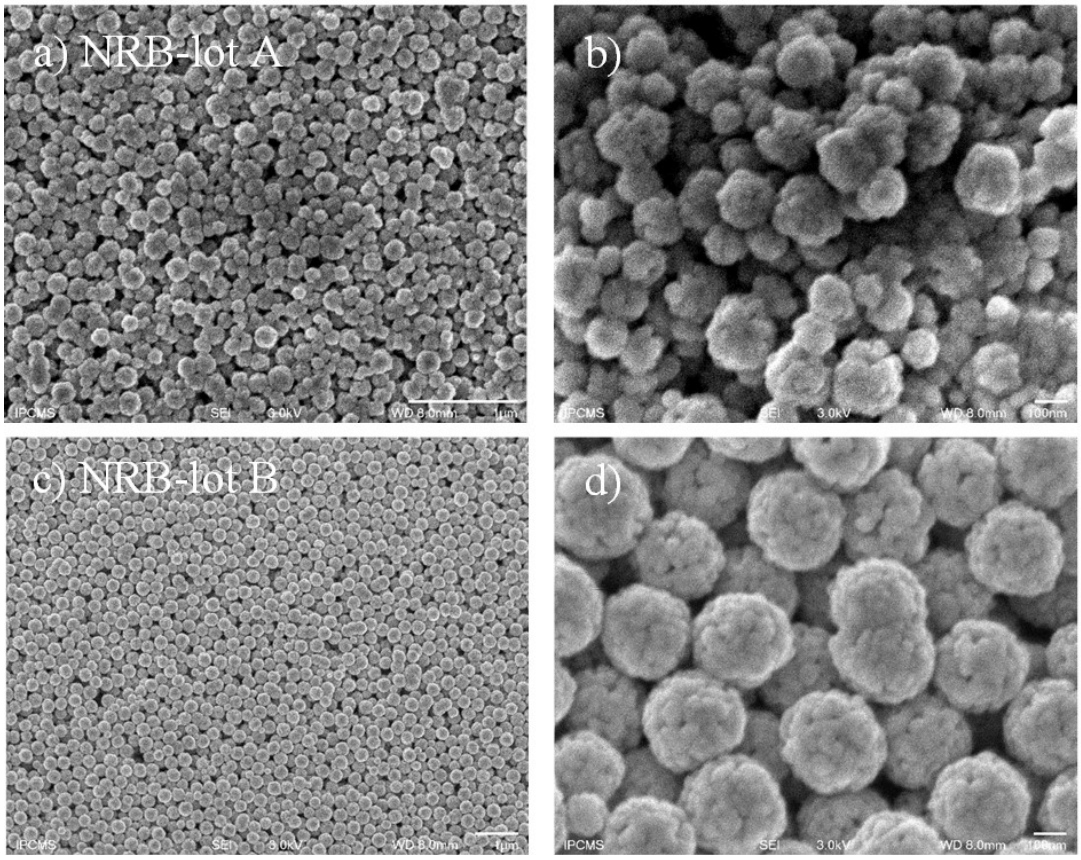

Figure 18: SEM images of two different lots –different hydration rate. a) and b) for RSN-lot A (RSN mean size=150 nm, grain size = 29 nm). c) and d) for RSN-lot B (RSN mean size=330 nm, grain size = 29 nm).

Typical solvothermal synthesis with different cooling times (**Figure 19**).

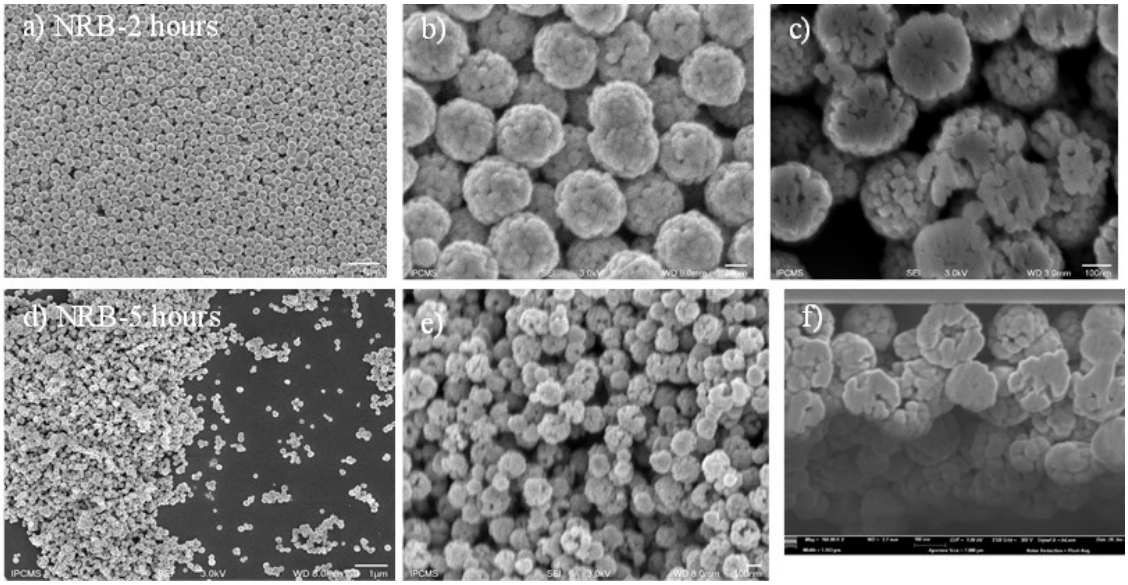

Figure 19: SEM images of RSNs after testing two different cooling times. a) b) and c) 2 hours represent RSN-full spheres (size 300 nm grain 30 nm). d) e) and f) for 5 hours represent hollow spheres (RSN size 300, grain 25 nm, hollow thickness 65 nm).

After cooling for 2 hours, RSN-full spheres are obtained with a mean size of 300 nm and constituted of grain with a mean size of 30 nm. Longer cooling time favours inverse Oswald ripening and thus hollow RSNs are obtained. The carbon coating of such hollow RSNs should be favorable for the expected applications.

(5-2) Synthesis of Mn or Zn doped RSN

The synthesis protocol is the same, excepting that XCl_2 (X=Mn, Zn) is added in order to dope the RSN. Different doping amount are tested.

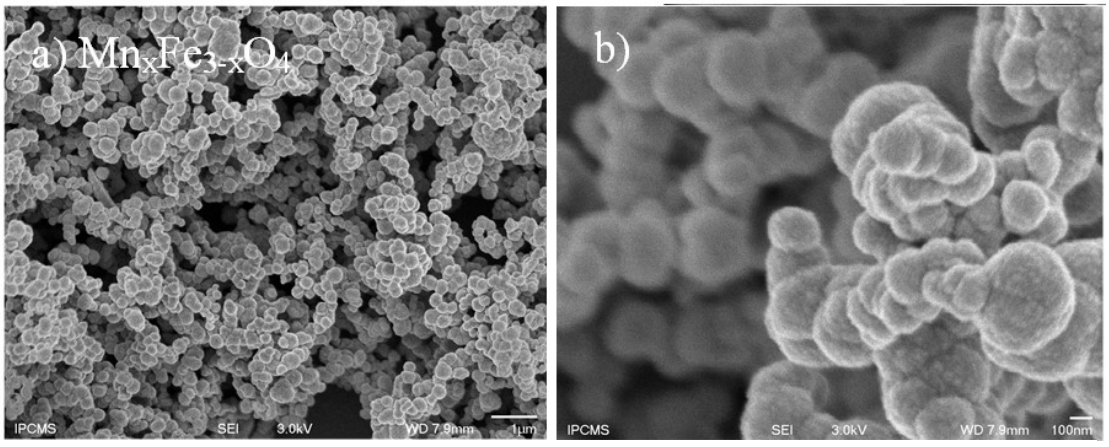

Figure 20: SEM images of Mn doped RSN.

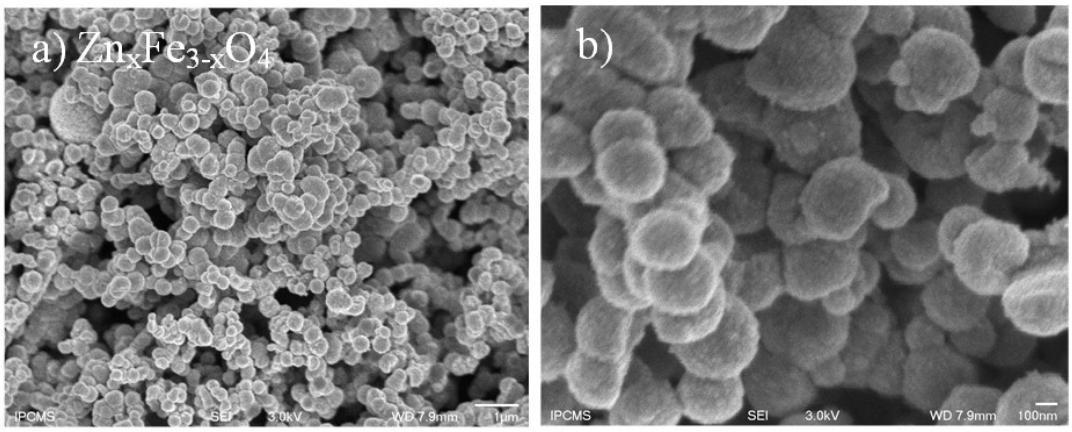

Figure 21: SEM images of Zn doped RSN.

The structural and magnetic characterizations are in course.

(5-3) Silica coating of RSN

In order to be better dispersed in the polymer matrix for magneto-dielectric measurement, the RSNs have been coated with a silica shell which can be further functionalized by silane molecules. This silica coating was not easy to proceed and different conditions have been tested such as a coating with hydrophobic ligand to place CTAB molecules at the surface of RSNs. After a bibliographic study, the most promising technique was to citrate at first the RSNs before growing the silica shell.

After synthesis, the surface of RSN have thus been modified using citrate trisodium. Using a modified Stöber reaction at room temperature, RSNs were then coated by a thin dense silica layer. A second shell of mesoporous silica was then deposited on via a surfactant template method.

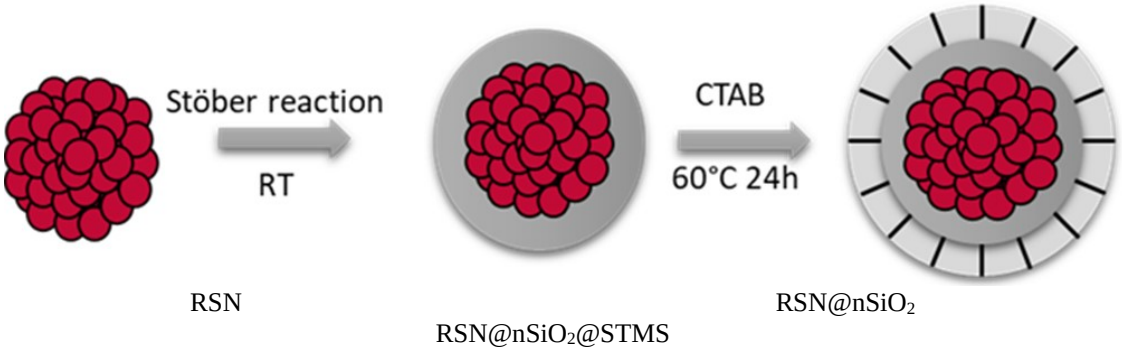

Figure 22: Schematic diagram for the synthesis of silica coated RSN.

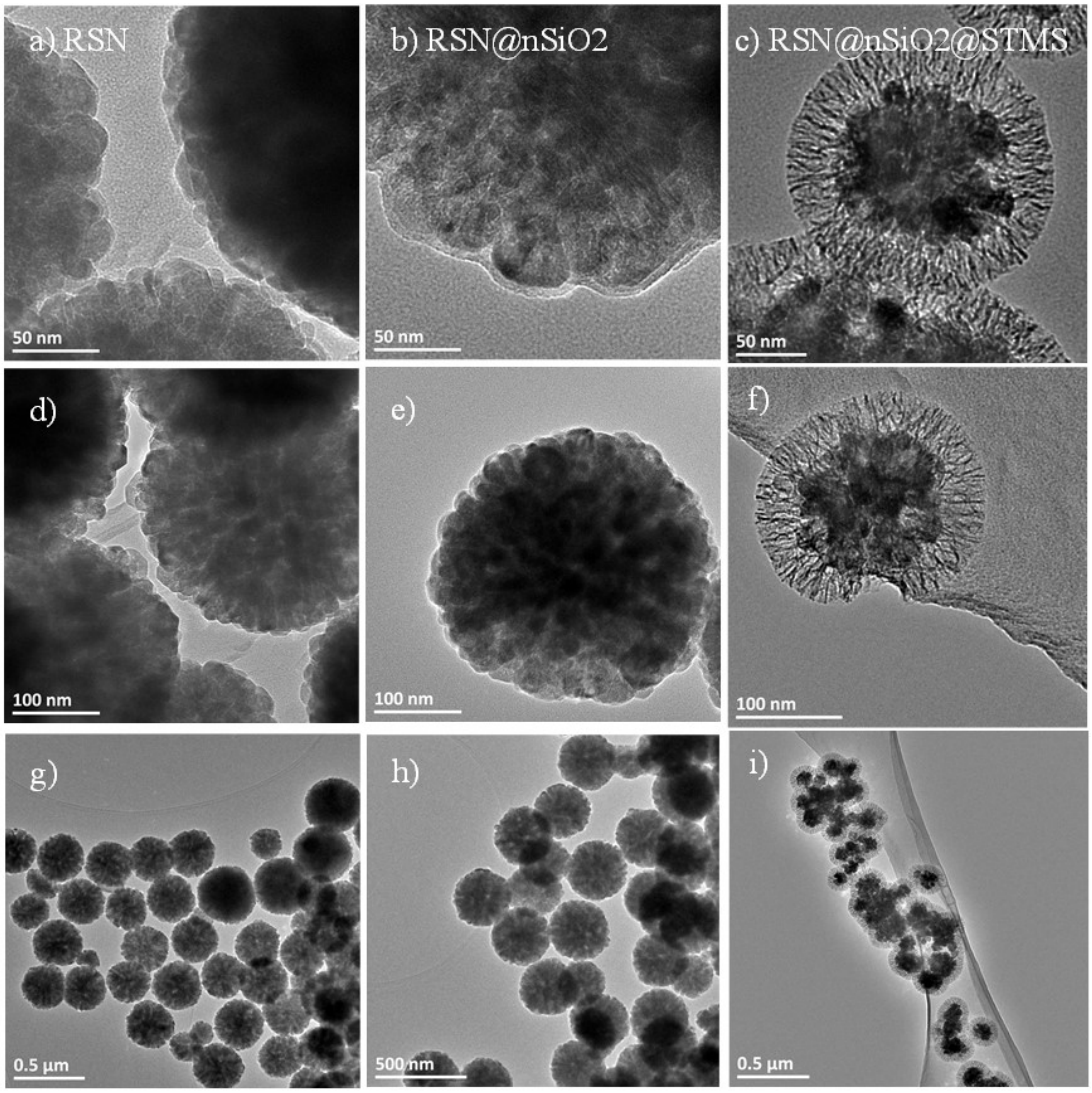

Figure 23: Typical TEM images (Synthesis of silica coated RSN).

(6) Prof. Peter Kofinas's group is working on magneto dielectric materials

Of the magneto-dielectric material studied by the Kofinas lab, those that use zero-valent iron (Fe^0) nanoparticle have shown the strongest magnetic properties (e.g. high saturation magnetization). To these particles, several surface coatings have been explored such as silica, titanium dioxide, and silver.[1,2] The polymer matrix material used has been polydimethylsiloxane. Although bulk Fe^0 has the highest theoretical saturation magnetization (M_s) of any material, the composites previously studied have exhibited significant reductions in M_s – compared to bulk Fe^0 – due to oxidation of uncoated Fe^0 nanoparticles or due to the interfacial interactions between the metallic core and its shell layer (i.e. silica, titanium dioxide).[3] In addition to these limitations, the strategy for mixing nanoparticles with polydimethylsiloxane (PDMS) can be problematic. PDMS is inherently viscous, making it impossible to mix in high concentrations of magnetic filler material without the addition of a solvent. If added, this solvent needs to be removed under vacuum, after mixing, to prevent the formation of air pockets in the material upon curing. This, combined with the long 4-hour cure time that was previously reported by the Kofinas lab, increases the probability for particle aggregation or settling. This, in turn, increases the likelihood of an inhomogeneous composite that will display subsequent anisotropy/inhomogeneity in magnetic, dielectric, and mechanical behavior. Therefore, the work currently undertaken has set out to improve on these limitations.

For this project period, we have worked towards developing a magneto-dielectric material with improved saturation magnetization, lower coercivity, and lower magnetic/dielectric loss. This work has taken two methods of approach for accomplishing these tasks, which were conducted in the following order: (1) investigating new magnetic filler materials with a higher saturation magnetization and a lower coercivity than the materials previously investigated, and (2) increasing the homogeneity of the composite by investigating different matrix materials and nanoparticles surface coatings. Several nanoparticle compositions are being investigated in our three laboratories, independently and through synergistic collaborative exchanges of students.

(6-1) New magnetic filler: iron-cobalt nanoparticles (Prof. Peter Kofinas's group)

Cobalt is known to possess a high magnetic moment so it was hypothesized that by alloying iron nanoparticles with this material, a larger saturation magnetization could be attained compared to particles of pure iron. After an extensive literature review, it was determined that a chemical reduction technique using hydrazine would be an optimal synthetic route to the formation of these alloyed FeCo particles due to the high M_s, low H_c, and uniform size/shape particles this synthesis yields.[4,5] The method used is summarized in Figure 10. In short, iron sulfate, cobalt chloride, poly(ethylene glycol), and hexane were mixed under inert atmosphere and heated to 78 °C. To this solution, a separate solution of water, sodium hydroxide, and hydrazine was added. Once adequately mixed, this new solution was transferred to a Teflon-lined autoclave and allowed to react for 3 hours at 120 °C. The particles were then collected and washed five times with water and five times with ethanol, using a strong magnet for separation in between washes.

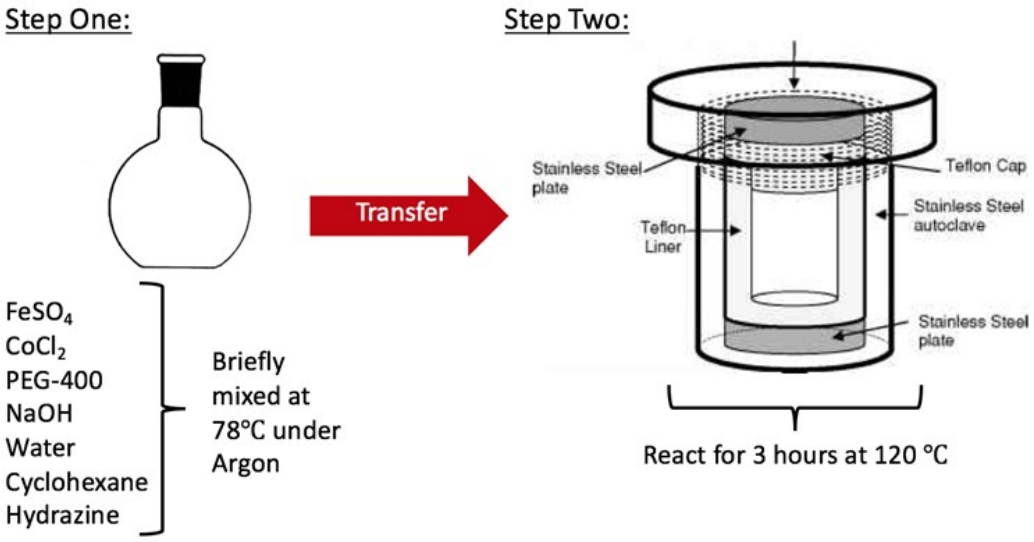

Figure 24: Overview of the synthesis used to attain magnetic FeCo nanocubes. Images taken from indiamart.com (left) and texaspowerfulsmart.com (right).

Several attempts, with modifications along the way, were used before attaining a product similar to what was previously reported. Initially, no autoclave was used in the reaction because some literature suggested that it was not necessary.[4] For this, the particles were allowed to react under reflux for 3 hours instead of transferring to an autoclave. This resulted in particles that had a substantially weaker magnetic attraction to the strong magnet during purification, compared to previous Fe^0-citrate particles synthesized. Furthermore, scanning electron microscopy (SEM) images showed that the particles created were very inhomogeneous in shape and size (Figure 11a). However, it is worth noting that several cubes were present, which was the expected particle shape for this synthesis. Given the weak M_s value and inhomogeneity of the shapes and sizes, the conclusion was that this approach would not produce a filler material with improved properties. Upon implementing the autoclave, the particles formed were very homogenous in shape and size, similar to results reported in literature (Figure 11b-c).

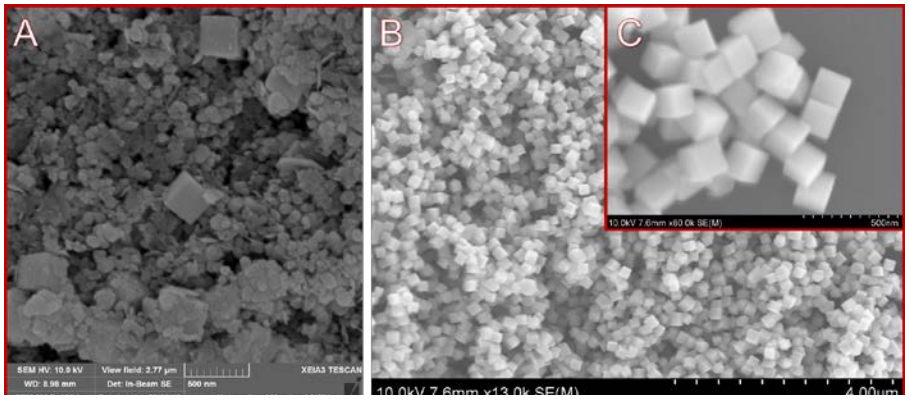

Figure 25: Scanning electron images of FeCo nanoparticles (A) formed without the use of an autoclave reactor and (B-C) with the use of an autoclave reactor.

In order to verify that the correct phases were present, x-ray diffraction was used. Samples from two separate syntheses were tested, both of which produced the same diffraction pattern as shown in Figure 12. This was done to verify the uniformity of each synthesis. The peaks attained were very well defined and identical to those previously reported for a cubic FeCo alloy, with reflections in the (110) and (200) planes.[4,5] It is also worth noting that no peaks indicative of an oxide phase are present. This is significant because oxidation is common for metallic nanoparticles syntheses, such as those conducted by Vural et. al in previous investigations by the Kofinas group.[1] Since oxides possess lower saturation magnetizations compared to their metallic counterparts, the lack of this phase in the nanoparticles allows for a higher saturation magnetization.

(6-2) Composite magnetic behavior

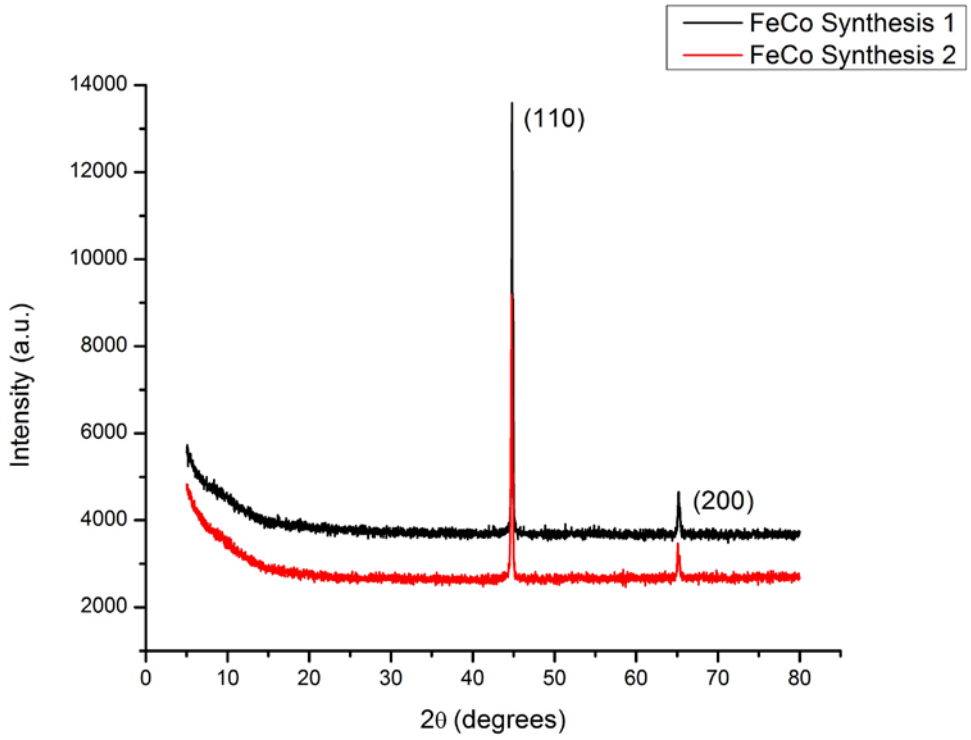

Figure 26: XRD diffraction pattern for two separate FeCo synthesis, both using an autoclave reactor. Data shifted vertically for clarity.

Upon the successful synthesis of FeCo nanocubes, these particles were then mixed into a PDMS polymer to form a composite material for magnetic testing. This was the initial choice in matrix material because the protocol for its use was well established by previous members of the Kofinas group (Figure 27A). However, as noted earlier, several limitations are associated with PDMS. For one, it is very viscous. This makes it difficult, if not impossible, to mix high wt% concentrations of nanoparticles without the use of a solvent (i.e. tetrahydrofuran) to lower the viscosity. This is problematic because if solvent is added, the solution must be placed under vacuum to remove the solvent in order to prevent air pockets from forming in the composite during the curing process. If this is not done, the dielectric behavior of the material will be altered. Consequently, by placing the material under vacuum, more time is introduced into the curing process to allow for particle agglomeration or settling. This can significantly affect the magnetic and dielectric properties of the material. For similar reasons, another downfall to using this polymer is the associated cure time of 4 hours, as reported in literature.[1,2,6] Once again, this time duration can result in particle aggregation and settling, changing the material's dielectric and magnetic properties.

A good indication of a homogenous composite film is whether or not it displays uniform magnetic behavior. Furthermore, the processing of these films should result in a magnetically isotropic material.

Deviations from isotropy could also indicate inhomogeneity. Utilizing a vibrating sample magnetometer, two different methods were incorporated to determine how well the composites were mixed. For one, two samples were tested from different regions on a single film (Figure 27B). Secondly, the sample was exposed to different orientations of the external field ($\vec{H}$) (Figure 27C), which gives an indication of magnetic anisotropy.

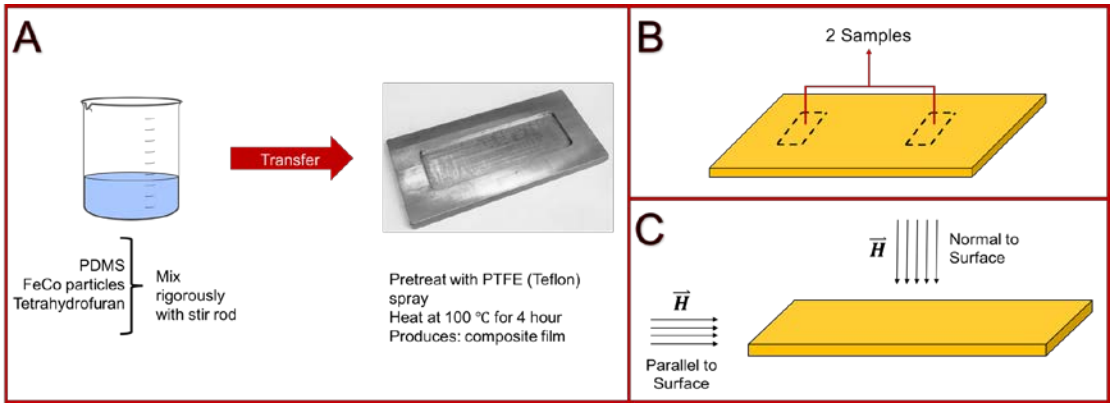

Figure 27: (A) Overview of method used to form composite sample using Sylgard 184. (B) Homogeneity of the sample was tested by taking two separate samples from a single composite and (C) by testing the magnetic properties of a single sample under different orientations of the applied magnetic field.

The results from the test method shown in Figure 27B can be seen in Figure 28A. The two samples show a significant difference in saturation magnetizations (Table 2), while the coercivities are relatively the same. As evident by the data, the sample is not magnetically homogeneous which strongly indicates an inhomogeneous distribution of nanoparticles. The results (Figure 28B, Table 2) from the test method shown in Figure 28C are also indicative of this. A likely explanation for why the sample shows a stronger M_s value for an applied field ($\vec{H}$) parallel to the surface is because the magnetic filler material settled at the bottom of the film during the curing process. This would result in a higher orientation of particles along a single plane (i.e. the bottom surface of the sample), compared to particle orientations perpendicular to the surface. Thus, this higher degree of orientation would result in a larger saturation magnetization for that direction due to an increase in magnetic dipole alignment of the nanocubes.

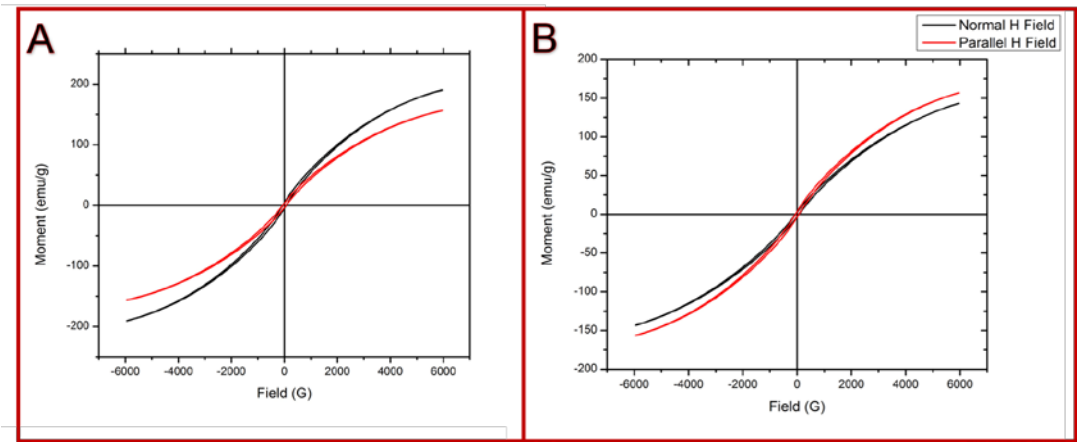

Figure 28: VSM results of an FeCo/Sylgard 184 composite. (A) Two samples were taken from different regions in the same material to test homogeneity and (B) a single sample was tested at two different orientations of the external magnetic field to test for anisotropy.

Table 2: Saturation magnetization and coercivity data taken from Figure 14.

	M_s (emu/g)	Coercivity (Oe)
FeCo Sample 1 (Figure 14A)	190	67
FeCo Sample 2 (Figure 14A)	157	65
Normal H Field (Figure 14B)	143	69
Parallel H Field (Figure 14B)	157	69

Despite this lack in uniformity between the sample, it is definitely worth noting that the region displaying the lowest saturation magnetization still showed a higher M_s value and lower coercivity than the Fe^0/citrate particles created from previously published synthetic methods by the Kofinas group (Figure 29, Table 3).[1] While it is still difficult to draw definitive conclusions, it can be expected that the new composites will have higher M_s values – and by association higher permeabilities – than the Fe^0 composites previously developed; since the M_s value for the FeCo nanocubes can be as high as 211 emu/g, as reported in literature.[5]

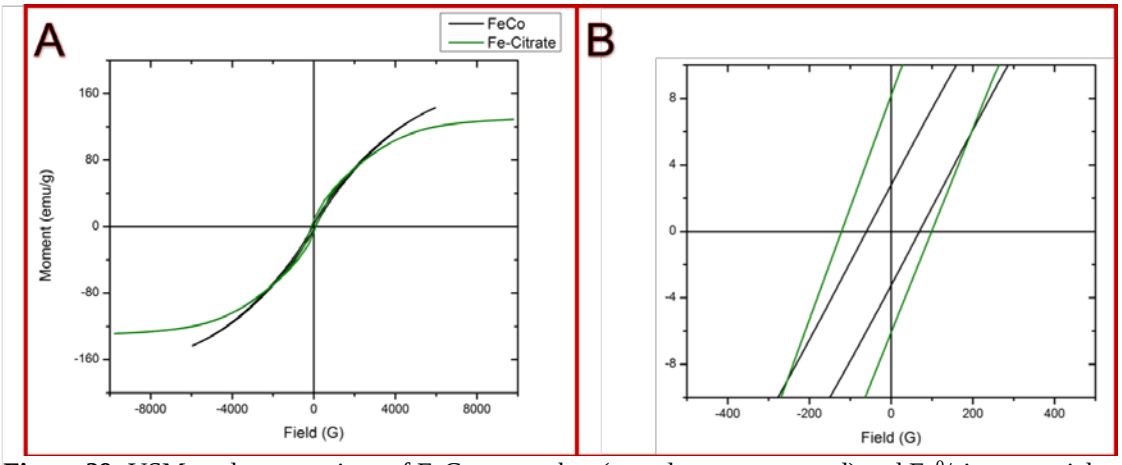

Figure 29: VSM study comparison of FeCo nanocubes (autoclave reactor used) and Fe^0/citrate particles previously investigated by the Kofinas lab. Figure A and B are of the same study but at different scales.

Table 3: VSM data of FeCo nanocubes (autoclave reactor used) and Fe^0/citrate particles. Data taken from Figure 15.

	M_s (emu/g)	Coercivity (Oe)
FeCo	143	69
Fe^0-Citrate	129	100

Conclusions and Future Work

The mechanism formation of porous raspberry shaped nanostructures synthesized by a one-pot polyol solvothermal method has been investigated in details from the early stages by using a combination of a wide panel of characterization techniques, namely SEM, TEM, XRD, FTIR spectroscopy, Mössbauer spectroscopy, elemental analysis, EELS and thermogravimetric analysis. A time resolved study demonstrates the intermediate formation of an amorphous iron alkoxide phase with a plate-like

lamellar (PLS) structure. We showed thus that the synthesis of RSNs involved two iron precursors : the starting one and this in-situ formed iron alkoxide precursor which decomposes with time and heating and contributes to the growth step of nanostructures. Finally, a formation mechanism of RSN from such an original PLS structure, which is commonly admitted to proceed through the oriented aggregation of nanocrystals, has been proposed. Such a study will allow to propose strategies to dope these RSNs with other elements such as Mn, Co, Ni or Zn to improve their magnetic properties.

Stretchable magneto-dielectric composites were prepared using collectively assembled iron oxid e nanostructures as fillers in an elastomer (polydimethylsiloxane) matrix. These raspberry-shape d nanostructures (RSNs), synthesized by a one-pot polyol solvothermal method, consist of orie nted aggregates of iron oxide nanocrystals (nanocrystals with common crystallographic orientati ons directly combined together to form larger ones), which ensure a very low oxidation state of Fe_3-xO_4 nanocrystals and lead to interesting magnetic properties. The oriented aggregation of nanocrystals generates a large interface between nanograins significantly reducing their surfa ce oxidation, improving crystal quality and preventing the formation of surface and volume sp in canting. Therefore these iron oxide RSNs display low coercivity with enhanced saturation magnetization (M_s). The use of such citrated RSN as filler material with improved magnetizati on and low coercivity allowed the fabrication of magneto-dielectric composites that can combi ne permeability values reaching 2.3 with magnetic loss values limited to 0.11. The resulting c omposites can also be stretched up to 165% strain before failure due to good adhesion betwe en the elastomer and citrate capped RSNs. In addition, the composition of these fillers was al tered to adjust the resonance frequency of the resulting composite material. Stretchable magnet o-dielectric composites consisting of maghemite-rich RSNs and magnetite-rich RSNs demonstra ted resonance frequencies similar to the spherical ferrimagnetic/ferromagnetic resonance of mag hemite and magnetite, respectively.

We have demonstrated that raspberry shaped magnetite nanostructures are very interesting and even key elements to fabricate flexible materials with low dielectric loss, high permittivity and permeability values at radio frequencies (1 MHz- 1 GHz). The permeability values achieved by composites made from collectively assembled corona magnetite nanoparticles are significantly higher than the existing magnetite-polymer composites and magnetite-PDMS composites. Additionally, the composites prepared with collectively assembled corona magnetite nanoparticles exhibit an extraordinary magnetic resonance, which changes with the particle size of magnetite nanoparticles. In contrast to these interesting and promising properties of the composites, the composites have high dielectric loss, which can be addressed easily by introducing an insulating layer around the magnetite nanoparticles. We believe such composites could be utilized for high-bandwidth radio frequency antennas as the dielectric loss values are further decreased.

We are currently aiming to identify the origin of the magnetic resonance by characterizing the material in a broader spectrum. Currently synthesis is performed to modulate the nanograin size or to dope the nanostructures with cobalt or manganese or nickel or zinc to modulate the magnetic properties. First experiments with cobalt showed that although similar saturation magnetizations have been obtained, the coercivity is larger as shown in the figure below. Other approaches would be to coat them with carboneous materials or silica or gold in collaboration with Dr Yuanzhe Piao.

Currently, the Kofinas group is working towards coating the FeCo nanocubes in silica. Since the backbone of the matrix polymer is comprised of silicon and oxygen, the chemical constituents of silica, it is hypothesized that a silica coating will allow for better mixing of the filler material and, thus, a more homogenous composite. The synthetic protocol used has been a modification of those reported in literature for the coating of other metallic nanoparticles (e.g. gold, platinum). [9,10,11] In brief, particles will be dispersed in ethanol and mixed with citrate. Then, the particles will be washed in ethanol to remove any excess citrate that did not coordinate with the nanocube surface. From there, the FeCo nanocubes will be re-dispersed in ethanol and brought to a pH of 10 with ammonium hydroxide. Tetraethyl orthosilicate will then be added in small batches and the particles will be allowed to react for 24 hours. Subsequently, verification needs to be conducted to ensure that the reaction was successful, which will be accomplished with TEM and SEM.

The Kofinas group is also currently working on better characterizing the cure rates of the new photocurable PDMS (p-PDMS) polymer, using various concentrations of DMPA. It is expected that with higher concentrations of photoinitiator, a faster cure rate is possible but at the expense of a material with a higher modulus and smaller strain at failure (i.e. more brittle). Therefore, tensile testing studies will need to be conducted in order to better elucidate the correlation between DMPA concentration and cure rate/mechanical properties. Once this is completed, the next step will be

introducing the FeCo particles into the polymer. This study will utilize both FeCo and FeCo@SiO_2 nanoparticles in order to determine how well each of these materials disperse within the p-PDMS matrix. Again, VSM will be used for characterization, as well as mechanical testing (i.e. tensile tests).
The RSNs doped with different amount of Zn and Mn (by Prof. Sylvie Bégin-Colin's group) will be characterized magnetically and the best samples will be coated with silica and send to Prof Peter Kofinas for dispersion in a polymer matrix and magneto-dielectric measurements. The doping of RSNs with rare earth elements is in course. Hollow RSN with different grain sizes and porosity will be send to Prof Yuanzhe Piao to coat them with carbon.

References:

1. Vural, M., Crowgey, B., Kempel, L. C. & Kofinas, P. Nanostructured flexible magneto-dielectrics for radio frequency applications. *J. Mater. Chem. C* **2,** 756–763 (2014).
2. Yang, T. I., Chuang, C. Y., Yang, S. C., Kempel, L. C. & Kofinas, P. Core/Shell Iron/Oxide Nanoparticles for Improving the Magneto-Dielectric Properties of Polymer Composites. *Adv. Eng. Mater.* **18,** 121–126 (2016).
3. Kong, L. B. *et al.* Recent progress in some composite materials and structures for specific electromagnetic applications. *Int. Mater. Rev.* **58,** 203–259 (2013).
4. Wei, X. W. *et al.* Large-scale controlled synthesis of FeCo nanocubes and microcages by wet chemistry. *Chem. Mater.* **20,** 6248–6253 (2008).
5. Yuan, J., Li, C., Liu, Z., Wu, D. & Cao, L. Synthesis of variously shaped magnetic FeCo nanoparticles and the growth mechanism of FeCo. 6506–6515 (2017). doi:10.1039/C7CE01353A
6. Vural, M. *et al.* Stretchable magneto-dielectric composites based on raspberry-shaped iron oxide nanostructures. *J. Mater. Chem. C* **4,** 2345–2352 (2016).
7. Sun, Y., Jiang, L. T., Okada, R. & Fu, J. UV-modulated substrate rigidity for multiscale study of mechanoresponsive cellular behaviors. *Langmuir* **28,** 10789–10796 (2012).
8. Jothimuthu, P. *et al.* Photodefinable PDMS thin films for microfabrication applications. *J. Micromechanics Microengineering* **19,** (2009).
9. Liu, S. & Han, M. Synthesis, functionalization, and bioconjugation of monodisperse, silica-coated gold nanoparticles: Robust bioprobes. *Adv. Funct. Mater.* **15,** 961–967 (2005).
10. Liu, S., Zhang, Z. & Han, M. Gram-scale synthesis and biofunctionalization of silica-coated silver nanoparticles for fast colorimetric DNA detection. *Anal. Chem.* **77,** 2595–2600 (2005).
11. Liu, S., Wong, Y., Wang, Y., Wang, D. & Han, M. Y. Controlled release and absorption resonance of fluorescent silica-coated platinum nanoparticles. *Adv. Funct. Mater.* **17,** 3147–3152 (2007).

List of Publications and Significant Collaborations that resulted from your AOARD supported project: In standard format showing authors, title, journal, issue, pages, and date, for each category list the following:

a) papers published in peer-reviewed journals

Bokyung Seo, Chaedong Lee, Donggeon Yoo, Peter Kofinas*, Yuanzhe Piao*, A magnetically recoverable photocatalyst prepared by supporting TiO_2 nanoparticles on a superparamagnetic iron oxide nanocluster core@fibrous silica shell nanocomposite, RSC Advances, 2017, 7, 9587–9595.

b) papers published in peer-reviewed conference proceedings,

c) papers published in non-peer-reviewed journals and conference proceedings,

d) conference presentations without papers,

Sylvie Begin-Colin* et al., Design of new hybrid metal oxide, European Materials Research Society Spring Meeting 2018 (EMRS 2018), Palais des congrès de Strasbourg (Strasbourg Convention Centre), France, 20180618.

Yuanzhe Piao*, Facile preparation of self-assembled metal oxide nanoparticles/carbon hybrid nanofilms using salt powder as separation medium, European Materials Research Society Spring Meeting 2018 (EMRS 2018), Palais des congrès de Strasbourg (Strasbourg Convention Centre), France, 20180618.

e) manuscripts submitted but not yet published, and
f) provide a list any interactions with industry or with Air Force Research Laboratory scientists or significant collaborations that resulted from this work.
   (1) Prof. Peter Kofinas has performed courses at Strasbourg (12h eq TD) as invited professor.
   (2) The PhD student of Prof Peter Kofinas: Rebecca Fedderwitz visited Prof. Sylvie Begin-Colin's laboratory from May to August 2018 and worked on the silica coating of metallic nanoparticles.
   (3) The PhD student of Prof Yuanzhe Piao, Chaedong Lee visited Prof. Sylvie Begin-Colin's laboratory and worked on the doping of RSNs.
   (4) Prof. Sylvie Begin-Colin's student, Paula Duenas Ramirez went in Korea in Yuanzhe Piao's Lab and worked on the doping and carbon coating of RSNs.
   (5) Prof. Sylvie Begin-Colin's Post-Doc, Geoffrey Cotin visited Prof Peter Kofinas's Lab in October to work on the dispersion of silica coated nanoparticles in the polymer matrix.

Attachments: Publications a), b) and c) listed above if possible.

DD882: As a separate document, please complete and sign the inventions disclosure form.

Important Note: If the work has been adequately described in refereed publications, submit an abstract as described above and refer the reader to your above List of Publications for details. If a full report (e.g. for any unpublished work) needs to be written, then submission of a final report that is very similar to a full length journal article will be sufficient in most cases. This document may be as long or as short as needed to give a fair account of the work performed during the period of performance. There will be variations depending on the scope of the work. As such, there is no length or formatting constraints for the final report. Keep in mind the amount of funding you received relative to the amount of effort you put into the report. For example, do not submit a $300k report for $50k worth of funding; likewise, do not submit a $50k report for $300k worth of funding. Include as many charts and figures as required to explain the work.